



2004

60362345

This is to certify that the
thesis entitled

TOPOGRAPHIC IMAGING OF TOOL WEAR IN MULTILAYER
COATED INSERTS

presented by

JORGE A. OLORTEGUI-YUME

has been accepted towards fulfillment
of the requirements for the

Master of Science degree in Mechanical Engineering



Major Professor's Signature

8/25/04

Date

LIBRARY
Michigan State
University

PLACE IN RETURN BOX to remove this checkout from your record.
TO AVOID FINES return on or before date due.
MAY BE RECALLED with earlier due date if requested.

DATE DUE	DATE DUE	DATE DUE

**TOPOGRAPHIC IMAGING OF TOOL WEAR IN MULTILAYER COATED
INSERTS**

By

Jorge A. Olortegui-Yume

A THESIS

Submitted to
Michigan State University
In partial fulfillment of the requirements
for the degree of

MASTER OF SCIENCE

Department of Mechanical Engineering

2004

ABSTRACT

TOPOGRAPHIC IMAGING OF TOOL WEAR IN MULTILAYER COATED INSERTS

By

Jorge A. Olortegui-Yume

The present study deals with the confocal imaging of tool wear in multi-layer coated inserts using Confocal Laser Scanning Microscopy (CLSM) as a means to obtain the tool wear evolution in a local level.

Steady-state turning experiments were carried out on 1045 steel bars with multi-layer coated inserts consisting of TiN /Al₂O₃ /TiCN deposited on a carbide substrate. Topographical images of the crater wear as well as orthogonal sections of the flank and crater wears as functions of machining time were obtained. After the Scanning electron microscope (SEM) image analysis a humped island of TiN coating material next to growing a crater of Al₂O₃ and steel traces were found. The maximum crater depth location was observed to move across the rake face with machining time. These unexpected features of crater wear seem to have their origin in the competition of the abrasive and dissolution mechanisms. Validations of the confocal results were performed using the SEM and the Atomic force microscope (AFM).

DEDICATION

To

The One who is and who was and who is to come

ACKNOWLEDGEMENTS

It is a pleasure to acknowledge Dr. Patrick Kwon, my academic advisor, for his guidance and instruction during the duration of this research work. His patience and mentorship contributed greatly to the completion of this thesis.

I wish to extend my gratitude to my dissertation committee members: Dr. Shirley Owens and Dr. Brian Feeny for their invaluable contribution to this dissertation through their advice and suggestions.

I would also like to point out the professionalism and friendship of Dr. Stanley Flegler, Dr. Joanne Whallon, Carol Fleger, and Ewa Danielewicz at the Center for Advanced Microscopy of Michigan State University.

My gratitude and love to Lucy, my wife, for her encouragement, love and hard work. I am more than thankful to my mother for all the sacrifice, support and godly love given to me during my whole life.

My thanks to my friends and co-workers Chee-Kuang Kok, Tim Wong and Yi-Chong Zeng for their kindness, help and understanding despite their hectic agenda.

TABLE OF CONTENTS

LIST OF TABLES	VII
LIST OF FIGURES	VIII
KEY TO SYMBOLS OR ABBREVIATIONS	XI
OVERVIEW	1
Chapter 1 : INTRODUCTION TO WEAR IN CUTTING TOOLS	3
1.1 <i>MACHINING TECHNOLOGY TERMS AND DEFINITIONS</i>	4
1.2 <i>PRINCIPAL FORMS OF TOOL WEAR</i>	7
1.3 <i>TOOL WEAR BEHAVIOR</i>	11
1.4 <i>TOOL-LIFE CRITERION AND TOOL LIFE</i>	12
1.5 <i>TOOL WEAR MECHANISMS</i>	14
1.6 <i>COATED CUTTING TOOLS</i>	19
Chapter 2 : INTRODUCTION TO ADVANCED MICROSCOPY	21
2.1 <i>MICROSCOPY BASIC DEFINITIONS</i>	22
2.2 <i>CONFOCAL LASER SCANNING MICROSCOPY (CLSM)</i>	27
2.3 <i>THE SCANNING ELECTRON MICROSCOPE (SEM)</i>	37
2.4 <i>THE ATOMIC FORCE MICROSCOPE (AFM)</i>	38
Chapter 3 : STATEMENT OF THE PROBLEM	40
3.1 <i>LITERATURE REVIEW ON SURFACE TOPOGRAPHY</i>	40
3.2 <i>LITERATURE REVIEW ON CLSM APPLICATIONS</i>	41
3.3 <i>RESEARCH FOCUS</i>	42
Chapter 4 : EXPERIMENTAL WORK	44
4.1 <i>MACHINING EXPERIMENTS</i>	44
4.2 <i>CONFOCAL MICROSCOPY DATA ACQUISITION</i>	50
4.3 <i>ELECTRON MICROSCOPY DATA ADQUISITION</i>	61
4.4 <i>ATOMIC FORCE MICROSCOPY DATA ADQUISITION</i>	64
Chapter 5 : RESULTS AND DISCUSSIONS	67
5.1 <i>VALIDATION OF THE CRATER SHAPE</i>	67
5.2 <i>CRATER WEAR EVOLUTION AND MEASUREMENTS</i>	68
5.3 <i>ATOMIC FORCE MICROSCOPE RESULTS</i>	86
5.4 <i>FLANK WEAR EVOLUTION AND MEASUREMENTS</i>	86
Chapter 6 : SUMMARY AND CONCLUSIONS	96

APPENDICES.....	98
APPENDIX A : SEM MERGED IMAGE OF CRATER WEAR	99
APPENDIX B: EDS SPECTRAL ANALYSIS AND X-RAY DOT MAPS.....	100
APPENDIX C : BSE IMAGES OF CRATER WEAR.....	103
APPENDIX D : X-RAY LINESCANS OF CRATER WEAR	107
APPENDIX E : 5X AND 50X OBJECTIVE DATA COMPARISON.....	111
APPENDIX F: ATOMIC FORCE MICROSCOPE IMAGES	115
APPENDIX G: BSE IMAGES OF THE FLANK FACE	122
BIBLIOGRAPHY.....	124

LIST OF TABLES

Table 4-1 Inserts and corners used in the experiments	46
Table 4-2 Geometrical dimensions of the SNMA 643 insert [35].....	48
Table 5-1 Crater areas measurements for all machining times.....	75
Table 5-2 Maximum crater depth location for all machining times.....	80
Table 5-3 Time evolution of slope values at the flank face for reference 300s....	90
Table 5-4 Time evolution of slope values at the flank face for reference 480s....	91
Table 5-5 Time evolution of slope values at the flank face for reference 720s....	92

LIST OF FIGURES

Figure 1.1 Orthogonal view of the machining process [1]	4
Figure 1.2 Feed and depth of cut [2]	5
Figure 1.3 Nomenclature for the geometry of single-point cutting tools [2]	6
Figure 1.4 Progressive wear observed in the most common cutting tools [4]	7
Figure 1.5 Schematic illustrations of catastrophic tool failures [4].....	8
Figure 1.6 Regions of tool wear in metal cutting [3]	9
Figure 1.7 Sketch of a worn tool during cutting [5]	10
Figure 1.8 Flank wear development with time(carbide tool at 1 m/s) [3]	12
Figure 1.9 Effect of cutting speed on tool flank wear [1].....	13
Figure 1.10 Some features of a single-point tool wear in turning [3]	14
Figure 1.11 Adhesive wear representation.....	15
Figure 1.12 Two body and three body abrasion.....	16
Figure 1.13 Model of diffusion wear after Nahermein and Trent [8]	18
Figure 2.1 Depth resolution using a 80X/0.90 objective in air at $\lambda=633$ nm [21] .	23
Figure 2.2 Simplified schematic of a conventional light microscope [21].....	26
Figure 2.3 Illustration of the objective lens and the focal plane.....	27
Figure 2.4 The confocal principle	29
Figure 2.5 A typical Laser Scanning Confocal system [25]	30
Figure 2.6 Z-stack computer rendering of a simplified sample.....	34
Figure 2.7 Simplified schematic of a phi-z section	35
Figure 2.8 Intensity profiles and its relation to surface position.....	35

Figure 2.9 Intensity profiles shapes.....	36
Figure 2.10 Simplified rendering of a 3D reconstruction	36
Figure 2.11 Simplified schematic of a SEM [21].....	38
Figure 2.12 Schematic of the AFM principle of operation [21].....	39
Figure 4.1 Clausing/Colchester variable speed lathe(Model 8033).....	44
Figure 4.2 Insert and toolholder arrangement.....	47
Figure 4.3 Geometry of a the SNMA 643 insert [35]	48
Figure 4.4 Reflection confocal image of the multi-layer insert cross section	49
Figure 4.5 Zeiss LSM 210 confocal microscope.....	50
Figure 4.6 References for alignment in the LSM 210 pictures	52
Figure 4.7 (a), (b) Five sections method (Isolines view).....	56
Figure 4.8 Reference locations for crater wear evolution	59
Figure 4.9 Evolution of the crater obtained overlaying the B-B sections	59
Figure 4.10 JSM-6400 Scanning Electron Microscope	61
Figure 4.11 Nanoscope III scanning probe microscope	66
Figure 5.1 (a), (b) Confocal views of the Vynil poxysiloxane replica	67
Figures 5.2 (a),(b) Features of the crater wear for the multi-layer coated insert	69
Figure 5.3 2D confocal images showing the evolution in time of the crater wear.....	70
Figure 5.4 Topographical views of the worn corners for all machining times	71
Figure 5.5 BSE image of a worn corner with the chemical elements observed.....	73
Figure 5.6 Plot of the crater areas evolution in machining time.....	76
Figure 5.7 Plot of the length and width evolution for the exposed Alumina area.....	76
Figure 5.8 Variation of the width limits position of the crater in time.....	77

Figure 5.9 Orthogonal sections obtained at the maximum crater depth location.79

Figure 5.10 Plot of the maximum crater depth location versus machining time ..81

Figure 5.11 Plot of the maximum crater depth versus machining time.....81

Figure 5.12 Time evolution of crater wear at the 300 s reference (5X objective) 83

Figure 5.13 Time evolution of crater wear at the 300 s reference (5X objective) 84

Figure 5.14 Time evolution of crater wear at the 720 s reference (5X objective) 85

Figure 5.15 Flank wear evolution at the 300 s reference (50X objective).....88

Figure 5.16 Flank wear evolution at the 480s reference (50 X objective).....88

Figure 5.17 Flank wear evolution at the 720 s reference (50X objective).....89

Figure 5.18 Plot of slopes 1 and 2 versus machining time (300 s ref.).....93

Figure 5.19 Plot of slopes 3, 4, and 5 versus machining time (300 s ref.).....93

Figure 5.20 Plot of slopes 1 and 2 versus machining time (480 s ref.).....94

Figure 5.21 Plot of the slopes 3, 4, and 5 versus machining time (480 s ref.).....94

Figure 5.22 Plot of slopes 1 and 2 versus machining time (720 s ref.).....95

Figure 5.23 Plot of slopes 3, 4, and 5 versus machining time (720s ref.).....95

KEY TO SYMBOLS OR ABBREVIATIONS

CLSM	Confocal Laser Scanning Microscopy
SEM	Scanning Electron Microscopy
BSE	Backscattered electrons
EDS	Energy dispersive spectroscopy
AAN	Average Atomic Number
AFM	Atomic Force Microscopy
SPM	Scanning Probe Microscopy
N.A.	Numerical aperture
FOV	Field of view
LSM	Laser Scanning Microscope
HSS	High Speed Steel
BUE	Built-up edge
TEM	Transmission Electron Microscopy
TiN	Titanium nitride
Al ₂ O ₃	Aluminum oxide
TiCN	Titanium carbonitride
WC	Tungsten carbide
MCDL	Maximum crater depth location
sfp _m	Surface feet per minute
d _z	Depth resolution (μm)
λ	Light source wavelength (μm)
z(x,y)	z matrix

I(x,y)	Intensity matrix
Zm	Maximum intensity position (μm)
M	Magnification
f	Focal distance (mm)
A1	Darkest crater area (μm^2)
A2	Crater area defined by the inland ad edge side limits (μm^2)
L	Length of A1 measured parallel to the trailing edge (μm)
W	Width of A1 measured parallel to the trailing edge (μm)
W1	Position of the edge side limit of the crater respect to the trailing edge (μm)
W2	Position of the inland side limit of the crater respect to W1 (μm)
W3	Position of the inland side limit of the crater respect to the trailing edge (μm)
Zmax	Maximum crater depth location (μm)
Xr	Reference respect to the minor cutting edge (μm)
Yr	Reference respect to the main cutting edge or trailing edge (μm)
X	Maximum crater depth location respect to the minor cutting edge (μm)
Y	Maximum crater depth location respect to the main cutting edge or trailing edge (μm) matrix

OVERVIEW

The automation of machining processes in different industrial applications is a growing trend that requires an advanced scientific methodology to predict tool wear. This methodology should include the development of a new wear model must be capable of predicting tool life with better accuracy than the conventional methods. The shift to the usage of this new methodology would mean a drastic reduction of the huge amount of experimental research and related costs. Two main issues are attached to the development of this new methodology: an improved understanding of the wear phenomenon and a meaningful way to measure it. So far, most of the published work is based on the measurement of average properties of wear (traditional method) rather than in a localized analysis of the phenomenon.

This study intends to enhance, if not start, a new trend in tool wear measurement by means of providing a local level approach. The present approach will include the analysis of crater wear topography, time evolution of orthogonal wear profiles in specific locations, specially in the maximum depth locations., and the elapsed-time flank wear profiles for the same locations.

A Confocal Laser Scanning Microscope (Zeiss LSM 210) was used in reflective mode to get the topographical imaging of craters in multi-layer coated inserts along with the cross sections in defined locations. The sectioning feature of this microscope allowed the gathering of the orthogonal sections in the trailing edge for the analysis of flank wear. All the measurements where obtained using the built in software that comes with the microscope. The use of a Scanning Electron

Microscope (SEM) was necessary in order to establish the limits of each layer in connection with the growing worn areas of the insert. Validation of the information obtained with a Confocal Microscope was done with an Atomic Force Microscope (AFM).

Chapter 1 : INTRODUCTION TO WEAR IN CUTTING TOOLS

Although many great efforts have been made to understand the nature of tool wear, it continues to have unsolved problems. The relevance of better solutions to these problems lies on the great economical impact such solutions bring to industry. In the meanwhile, companies have to continue dealing with the four main economical effects of tool wear: Lower workpiece quality due to the deterioration in finish and dimensional accuracy, the damage on expensive work pieces if the cutting edge fails catastrophically, the cost of changing cutting edges and tools, and the increased power consumption due to excessive plasticity. Assuming that a complete understanding of the wear phenomenon was at hand, tool life could be more clearly defined and predicted, therefore, the economical effects could be minimized.

All the ongoing work in tool wear is oriented to three fundamental goals: (1) reliable prediction of tool wear, (2) *in situ* wear detection from measurements, and (3) wear prevention by the development of a new tool. The focus of the present study is to provide a micro-level approach for a better understanding of wear topography and wear measurement, which eventually will lead to the accomplishment of the first goal while giving a better understanding with the second.

1.1 MACHINING TECHNOLOGY TERMS AND DEFINITIONS

Machining is a manufacturing process in which a cutting tool is used to remove excess material from a workpart so that the remaining material is the desired part shape. The predominant cutting action involves shear deformation of the work material to form a chip; as the chip is removed, a new surface is generated. The machining process is most simply illustrated orthogonally (figure 1.1).

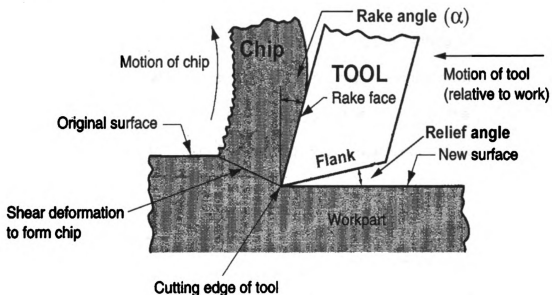


Figure 1.1 Orthogonal view of the machining process [1]

To perform the machining operation by removal of the chip, a relative motion is required between the tool and the work. In orthogonal machining operations, this motion is achieved by means of a primary motion, called the speed, and a secondary, motion called the feed. The shape of the tool combined with its penetration into the workpiece, combined with these motions, produced the desired shape of the resulting work surface [1].

1.1.1 CUTTING CONDITIONS

In general, an actual machining operation is much more complex, requiring the combination of cutting speed (v), feed (f) and depth of cut (d), which are called the cutting conditions, to control the process (figure 1.2). The speed at which primary motion is accomplished is known as *cutting speed* (v) and is expressed in feet /min (sfpm) or m/min. The *feed*, (f) is the lateral movement across the work to provide the secondary motion and comes expressed in inch/rev or mm/rev. The *depth of cut* (d) is the penetration of the cutting tool below the original surface of the workpiece. This is expressed in inches or mm. Additional descriptions needed to depict the geometry of a tool include the *Side cutting edge (or Approach) angle*, the *End cutting edge angle* and, the *corner or nose radius*.

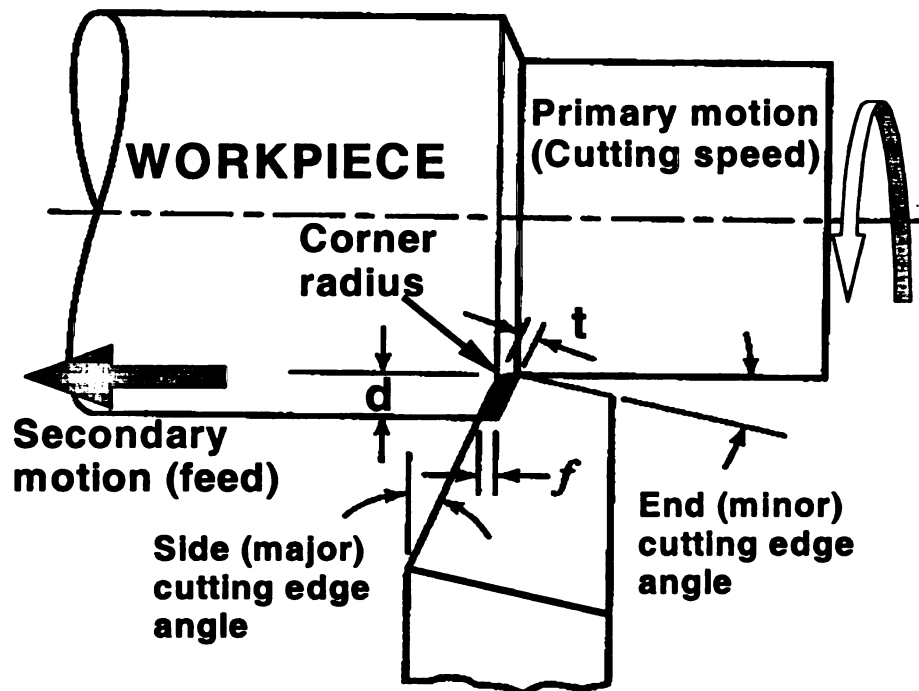


Figure 1.2 Feed and depth of cut [2]

1.1.2 GEOMETRY OF A SINGLE POINT CUTTING TOOL

A single-point cutting tool must accommodate not only for the primary motion but also allow for feeding and chip disposal. Therefore, the cutting edge is generally inclined and the chip is wound into a helix rather than a spiral. The tool is relieved both in the direction of feed and on the surface that touches the newly generated surface, which originates major and minor flank surfaces respectively. Intersections of these with the rake face constitute the major and minor cutting edges. The nose is rounded with adequate radius. The rake angle should be really measured in a plane perpendicular to the major cutting edge. However, for convenience, all angles are measured with respect to the major axes of the tool (figure 1.3).

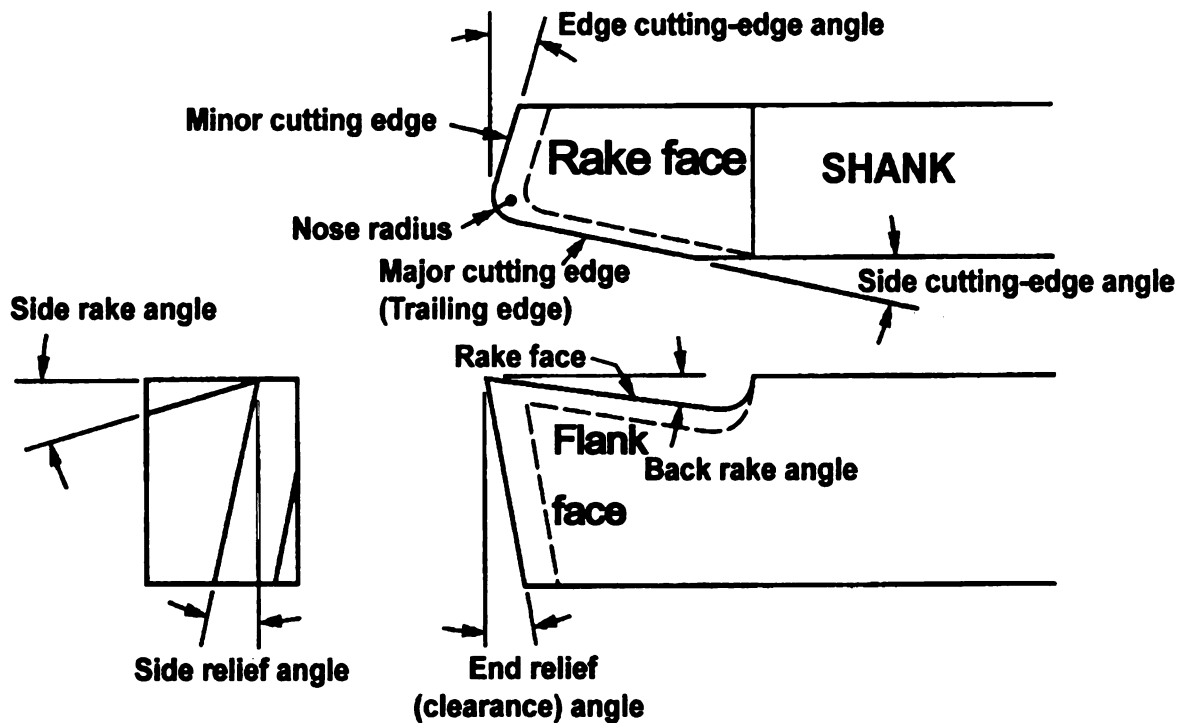


Figure 1.3 Nomenclature for the geometry of single-point cutting tools [2]

1.2 PRINCIPAL FORMS OF TOOL WEAR

Several ways in which the tool life can be brought to an end are possible. They may be classified into two main groups: the gradual and progressive wear at certain regions such as the rake face and flank face of a cutting tool, and catastrophic failures bringing the life of the tool to a premature end [3].

1.2.1 Typical wear of a single-point cutting tool

In figure 1.4, the progressive wear of the three most common cutting tools is shown. Note the particular behavior of crater and flank wear of different type of inserts [4]. In the same fashion, catastrophic failure is typical of the particular tool material (figure 1.5).

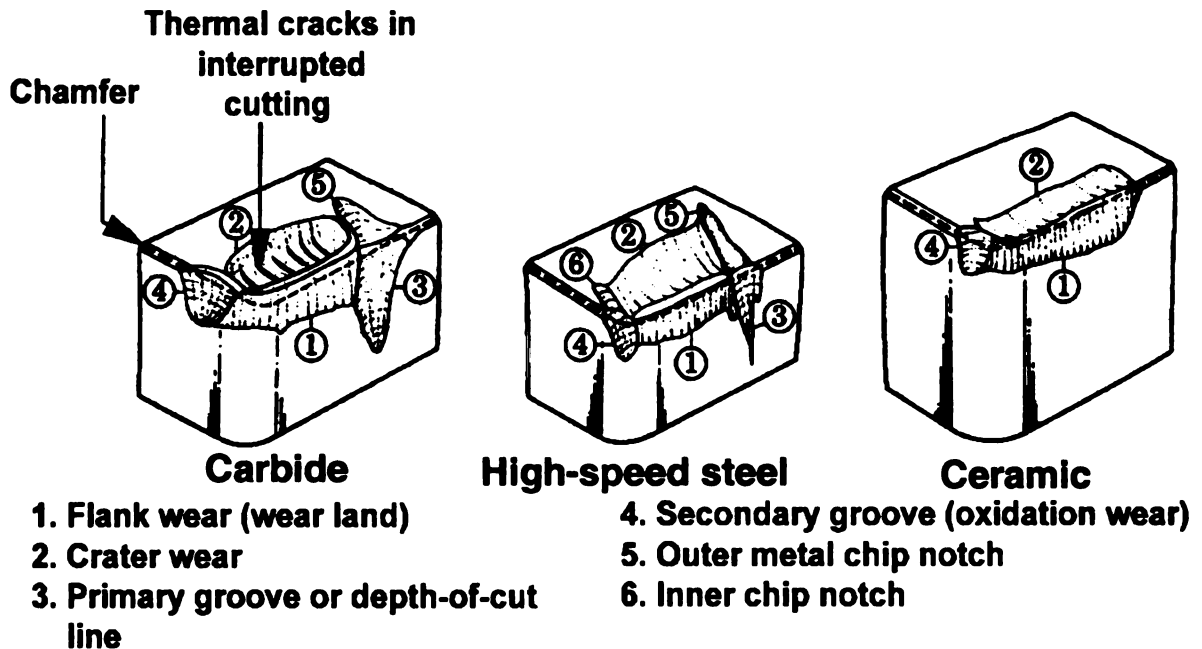


Figure 1.4 Progressive wear observed in the most common cutting tools [4]

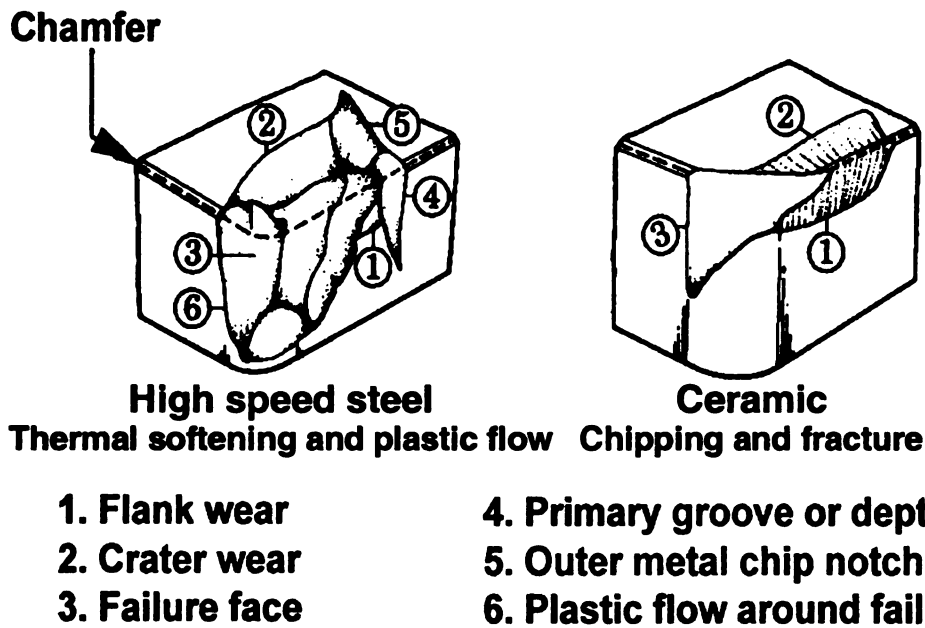


Figure 1.5 Schematic illustrations of catastrophic tool failures [4]

1.2.2 Types of progressive wear in metal cutting

The progressive wear of a tool takes place in two distinct locations: wear on the rake face characterized by the formation of a crater (thus called crater wear) and resulting from the action of the chip flowing along the face, and wear on the flank face (thus called flank wear) where a wear land is formed from the rubbing action of the newly generated workpiece surface [3]. Figure 1.6 gives a typical diagram for tool wear analysis.

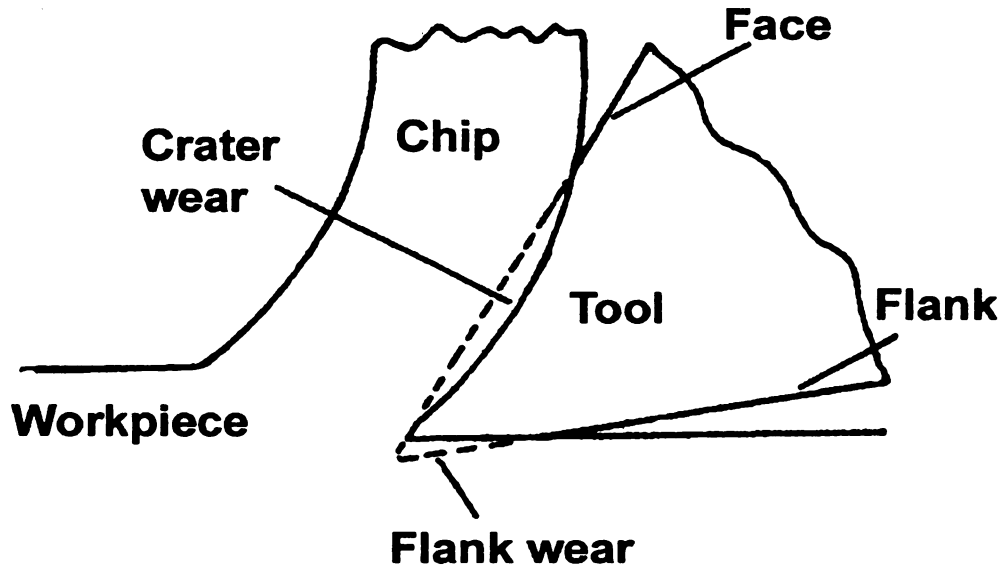


Figure 1.6 Regions of tool wear in metal cutting [3]

Also, figure 1.7 sketches clearly the connection between the 3D view of the worn tool and an auxiliary 2D section (A-A) following the direction of the chip flow.

1.2.3 Crater wear

The crater formed on the tool face conforms to the shape of the chip underside and is restricted to the chip-tool contact area (figure. 1.6). In addition the region adjacent to the cutting edge where sticking friction or a built-up edge (BUE) occurs is protected, resulting in relatively slight wear. In experimental work the maximum depth of the crater is used to measure the extent of crater wear and can be determined by a surface-measuring instrument such as a profilometer [3]. At very-high-speed cutting conditions, crater wear is often the factor that determines the tool life: cratering can become so serious that the tool edge weakens and eventually fractures.

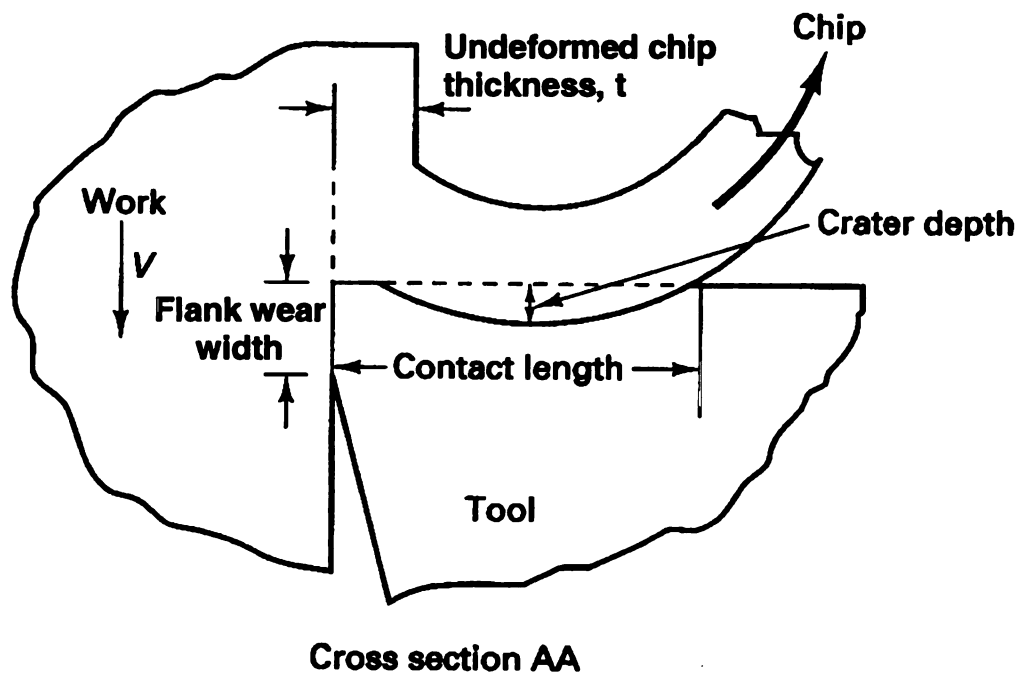
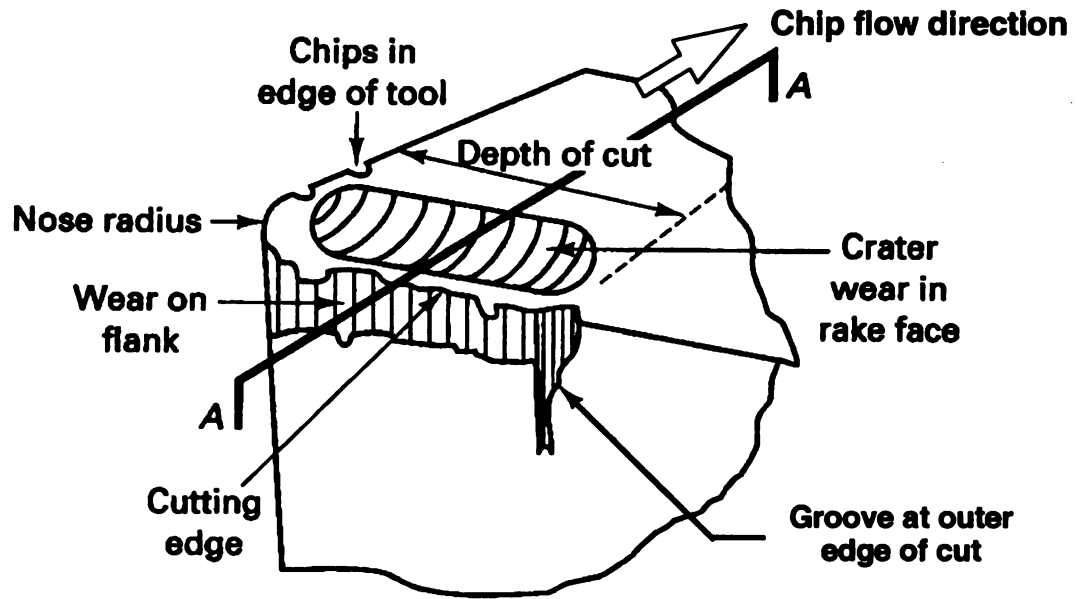


Figure 1.7 Sketch of a worn tool during cutting [5]

1.2.4 Flank wear

The rubbing of the tool flank face with the freshly machined surface causes the flank wear of a tool. Due to the rigidity of the workpiece, the worn area (flank wear land) must be parallel to the resulting cutting direction. The width of the wear land, which is accepted to measure the extent of flank wear, can be detected with a toolmaker's microscope. When tools are used under normal cutting conditions (economical conditions), the flank wear of a tool is usually the controlling factor for tool life [3].

1.3 TOOL WEAR BEHAVIOR

The general relationship of tool wear versus cutting time is shown in figure 1.8. Even though the relation is depicted for flank wear, a similar relationship occurs for crater wear [7]. The curve can be divided into three regions: the region AB where the sharp cutting edge is quickly broken down and a finite wear is established. This break-in period occurs within the first few minutes of cutting [1]. The region BC progresses at steady-state rate, thus depicted with a straight line, even though some deviations occur in actual machining. In the failure region CD, wear occurs at a gradually increasing rate. In this region the wear begins to accelerate and the general efficiency of the machining process is reduced. If the machining process is allowed to continue, the tool finally fails by temperature failure (plastic deformation and loss of the sharpen edge). Region CD is thought to indicate the region where the wear of the cutting tool has become sensitive to the increased tool temperatures caused by the presence of a wear land of large

proportions. Clearly, in practice it would be advisable to regrind the tool or to replace the insert before the wear enters the failure region [3].

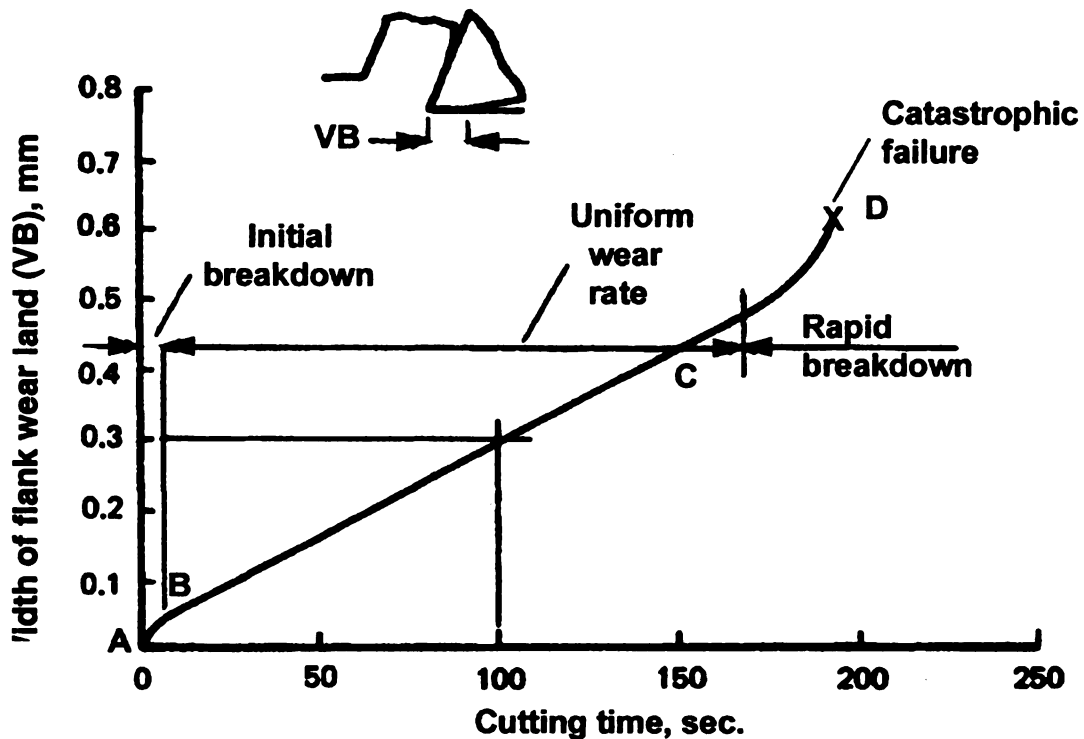


Figure 1.8 Flank wear development with time(carbide tool at 1 m/s) [3]

1.4 TOOL-LIFE CRITERION AND TOOL LIFE

A *tool-life criterion* can be defined as the predetermined threshold value of a tool wear measure or the occurrence of a catastrophic phenomenon. In the former, which is a more convenient definition, a predetermined level of tool wear is chosen so that when this level is reached the tool should be replaced or resharpened [3]. In the latter, the tool is operated until its failure occurs (final points of the curves in fig 1.9). This criterion has the economical disadvantages

associated with sharpening the tool that failed or the workpiece finishing quality.

Tool life is the cutting time required to reach a tool life criterion. In figure 1.9, a value of 0.020 inches in flank is established as a tool life criterion and three different tool lives are obtained for three different cutting speeds

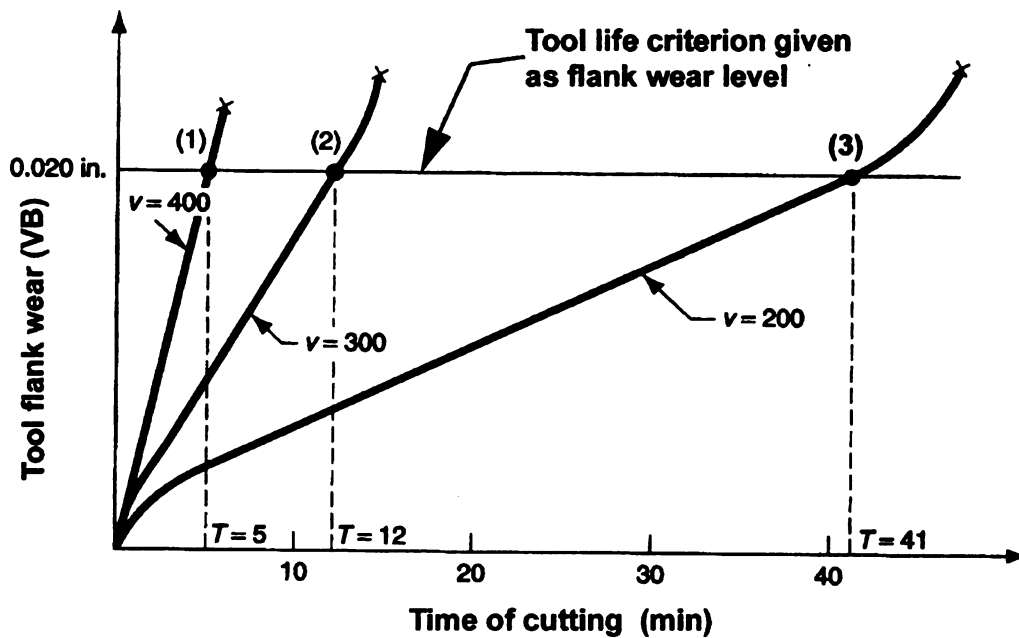


Figure 1.9 Effect of cutting speed on tool flank wear [1]

In practical machining operations flank and crater wear are not uniform along the active cutting edge. Therefore, it is necessary to specify the locations and degree of the wear when deciding on the extent of wear allowable before regrinding the tool, that is the tool-life criterion. Figure 1.10 shows the typical measurements recommended by ISO 5th Draft proposal [6].

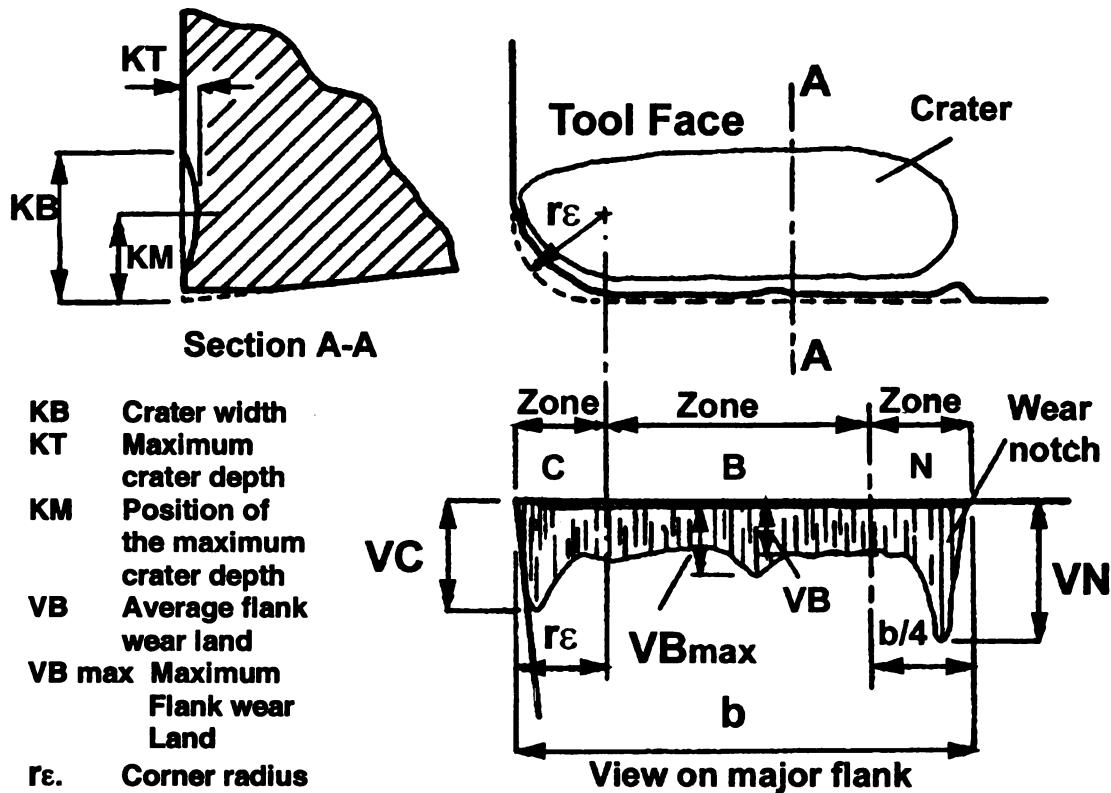


Figure 1.10 Some features of a single-point tool wear in turning [3]

1.5 TOOL WEAR MECHANISMS

Tool wear mechanisms may be classified into two categories: mechanical and chemical wear. Adhesive wear, abrasive wear, delamination wear and erosive wear are examples of mechanical wear, while diffusion, dissolution and corrosive wear are examples of chemical wear. In practical situations, however, tool wear may not be the result of one of these mechanisms acting independently, but a combination of two or more of them.

1.5.1 Adhesive Wear

In adhesive wear the chip and the tool come close enough together to form strong bonds. A particle transfer between the surfaces may take place if the bonds are stronger than the local strength. When this has happened several times a wear particle may leave the system after loosened from the tool [7]. These small fragments can be carried away on the underside of the chip or in the freshly generated surface (figure 1.11).

Adhesion wear is reduced at low cutting temperatures due to the lower adhesion. At high temperatures the thermal softening behavior will diminish adhesion: failure at high temperatures changes from within the tool to the interface or to within the tool or chip. Adhesion wear may be most active at intermediate temperatures [8].

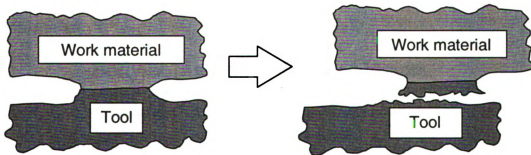


Figure 1.11 Adhesive wear representation

1.5.2 Abrasive wear

Abrasive wear occurs when hard particles on the underside of the chip slide against the tool face and remove tool particles mechanically. The hard particles on the chip may be formed by strain-hardening processes), chemical reaction of the wear debris, or may be hard constituents in the work material. Abrasive wear depends on the relative hardness between the tool and the abrasive particles and the distance cut. The harder the tool with respect to the abrasive particles the lower the abrasive wear [3]. The extent of abrasive wear also depends on the distance cut and can be described by Archard's wear law [8]. This law states that after some running-in period wear increases in proportion to cut distance. Typically, abrasion occurs in two forms known as 2-body abrasion and 3-body abrasion. In the former, hard inclusions in the chip penetrate and scratch the tool surface; in the latter, the confined hard, inclusions roll and slide on rake face of the tool scraping out tool material. In figure 1.12 the two types of abrasive wear are represented.

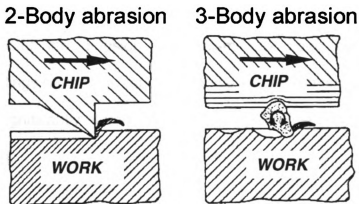


Figure 1.12 Two body and three body abrasion

1.5.3 Diffusion wear

The diffusion mechanism in solid state is the transportation of atoms from regions of high atomic concentration to regions of lower concentration within a crystal lattice. The local temperature controls the diffusion process and the diffusion rate increases exponentially with temperature [3]. Furthermore, the diffusional transport depends on the chemistry and structure of the materials, temperature, time, and the concentration gradient of the diffusing species [7]. In metal cutting, atoms move from the tool face to the chip. The continuous diffusion of atoms from the tool into the chip will weaken the surface structure of the tool in a very narrow reaction zone. [7] Chemical decomposition of a component of one of the sliding surfaces usually accompanies diffusion wear. This may increase the wear rate if the new component has strong affinity with the chip. In figure 1.13 a model of diffusion wear proposed by Naerheim and Trent [9] is shown. This model proposed that the wear rates of both WC-(Ti, Ta,W)C-Co(P-grade) cemented carbides are controlled by the rate of diffusion on Tungsten (and Ti and Ta) and carbon atoms together into steel.

The existence of the diffusion mechanism has been questioned but no categorical findings have been reported. However, if the mechanism exists at all, it contributes significantly at very high cutting speeds (beyond the normal cutting conditions) [10].

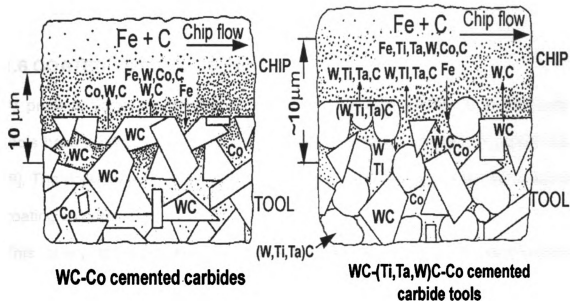


Figure 1.13 Model of diffusion wear after Nahermein and Trent [8]

1.5.4 Dissolution wear

This tool wear mechanism has been accepted in the last decade to influence crater wear, especially at high speeds [11]. Thermodynamical instability at high temperatures during machining causes the tool material to dissolve into the chip. Kramer and Suh [12] showed an outstanding correlation between wear predicted theoretically and those obtained in experiments. They consider crater wear as an equilibrium process of dissolution. A thermodynamical potential was considered for the solution of the tool material in the work material. This approach was completely opposite to that of thermal diffusion, known to be a non-equilibrium process and at that time was widely accepted as the main cause of crater wear.

Kramer and Suh [12], also proved that diffusion kinetics were relatively slow at normal cutting speeds.

1.6 COATED CUTTING TOOLS

At present, various estimates indicate that approximately 80 % of the cutting tools have a certain type of surface coating, and with a continuing growth trend [8]. The popularity of coated tools resides in the enhanced tool life that a surface coating can provide

This ability to resist wear comes from the concurrence of wear-resistant properties of both, the coating and the substrate. In general, coated cutting tools have a ceramic coating layer that provides excellent tribological properties and the cemented carbide or high-speed steel substrate that provides toughness. Moreover, coated tools must meet another requirement, compatibility between coating and substrate [10]. It follows then, that coatings and substrate must possess some desirable properties. In order to accomplish a good performance, coating layers must have: high hardnesses at high as well as low temperatures, good chemical stability, a porosity-free surface, possess a low coefficient of friction with respect to the materials machined, a good adhesion to the substrate, high productivity [13]. On the other hand, a substrate must possess: a good toughness, high hardness, compatible chemical composition respect to the coating, good thermal characteristics to withstand high temperature deposition, a coefficient of dilatation comparable to that of the coating, and good thermal conductivity.

The principal effect of the coatings is to serve as a diffusion barrier of tungsten in carbide tools. This will reduce the cutting temperatures by decreasing the friction coefficient and thereby reducing the cutting forces on the face of the tool. [14]. Coatings are made to be extremely hard and resistant to abrasion, hence they are not easily removed. Tool life is significantly increased by the lower temperature operations [15-17]. Cutting conditions and substrate properties play a main role in the increased tool life of coated carbides [14]. Early disintegration of coatings, as a result of thermal softening and plastic flow, are common at high speeds and especially with High Speed Steels (HSS) substrates. Nevertheless, it has been reported that *“under less severe conditions of lower feed rate, the ceramic coating can give a cutting life of ten times that of the uncoated tool [18]”*. For cemented carbide substrates, the tool wear is decreased as the hardness of substrate increases, because deformation of the cutting edge is smaller in a hard substrate [19].

Chapter 2 : INTRODUCTION TO ADVANCED MICROSCOPY

In the second half of the twentieth century, the convergence and integration of developments in optics, computer science, electronics, materials science, and molecular biology contributed greatly to huge improvements in microscopy. Non-destructive, non-invasive, and high-resolution imaging are some of the most important virtues of the new advanced microscopy. The most common technologies used in advanced microscopy include: Confocal Laser Scanning Microscopy (CLSM), Scanning Electron Microscopy (SEM), Transmission Electron Microscopy (TEM), Atomic Force Microscopy (AFM), and Scanning Tunneling Microscopy (STM).

In particular, CLSM possesses three remarkable characteristics. First, most confocal systems are capable of both confocal and conventional imaging. Second, the CLSM lateral resolution obtainable is approximately 170 nm, which is somewhere in between the resolution of a conventional light microscope (at 200nm) and an electron microscope (at 3-6nm) [20]; besides that, the depth resolution (3dB depth response) of a CLSM is approximately three times better than that of an SEM [21]. . Third, the CLSM is inexpensive when compared to the scanning electron microscope or other microscopes with similar technology.

2.1 MICROSCOPY BASIC DEFINITIONS

Many of the design principles of the confocal microscope are based upon the conventional light microscope [21], which is relatively simple when compared to the other systems used in advanced microscopy. Thus, a natural way to get acquainted with microscopy terminology is to begin with conventional microscopy terms.

2.1.1 Field of view

The field of view (FOV) is the diameter of the circle of light that can be seen when looking into a microscope. As magnification grows the FOV decreases [22].

2.1.2 Resolution

Generally speaking resolution is the ability of a system, or of a component, to distinguish fine detail. Two different types of resolution are commonly needed: transversal and depth resolution. Transversal resolution is usually defined as the smallest distance between two points in a plane parallel to the focal plane, which can be regarded as two different entities [20,23]. Whereas, depth resolution (d_z) is defined as the distance in the optical axis between half-power points (3-dB points) of the intensity response (figure 2.1) and is given by the approximate formula:

$$d_z (3dB) \approx \frac{0.89 \lambda}{(N.A.)^2} \quad \dots (2.1)$$

Where, λ is the wavelength of the light source and N.A. is the numerical aperture of the objective

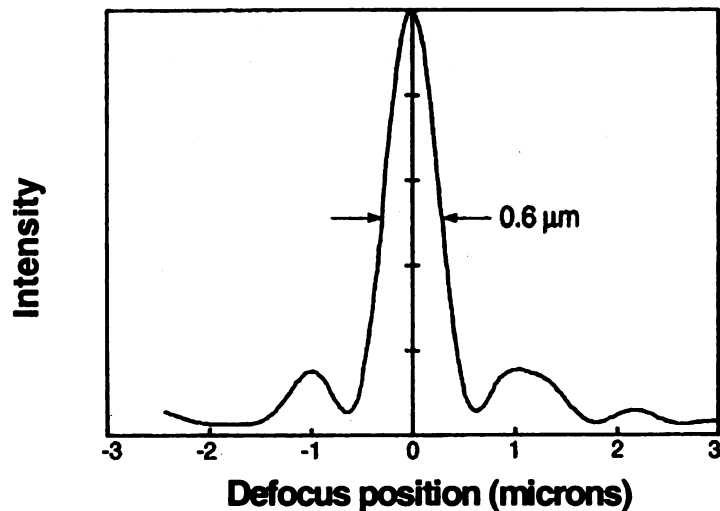


Figure 2.1 Depth resolution using a 80X/0.90 objective in air at $\lambda=633$ nm [21]

In confocal microscopy, the definition of resolution largely depends on the type of sample and which measurements are important to the observer. When imaging integrated circuits, for example, height differences of planar surfaces and the profiles of structures are the features of interest, then, depth discrimination and edge response are relevant to define resolution. In biological science, a depth-resolution definition based on point reflectors is more adequate to characterize the scattering from individual cells. Also, for biological samples is better to define transverse resolution with the idea of two close points being distinguished.

2.1.3 Magnification

Magnification represents how many times the primary image of the object is enlarged to become the final image. The magnification defines the size of the image at the detector. The total magnification in a microscope is a compound quantity. Each lens in the light path will increase or decrease the image. In the schematic shown in figure 2.2, the objective lens and the eyepiece will give their independent magnification to modify the final value of magnification. The magnification in the transverse direction for a simple lens (objective lens) is given by:

$$M_T = -d_i / d_o \quad \dots (2.2)$$

Where d_i is the tube length (the distance of the intermediate image plane from the back focal plane of the objective), d_o the distance of the sample object from the front focal plane of the objective. The negative sign accounts for the image inversion produced by a simple lens. Also, the longitudinal magnification comes as the square of the transverse magnification:

$$M_L = -M_T^2 \quad \dots\dots\dots(2.3)$$

. The eyepiece magnification is defined as the ratio of the size of the retinal image as seen through the instrument to the size of the retinal image as seen by

the unaided eye at a normal viewing distance of 250 mm [24]. The formula used to determine the eyepiece magnification is:

$$M_E = 250\text{mm}/f \quad \dots(2.4)$$

Where f stands for the focal length of the eyepiece lens. Finally, the total magnification of the system, M_R , will be given by:

$$M_R = M_T M_E \quad \dots(2.5)$$

2.1.4 Numerical Aperture (N.A.)

The numerical aperture (NA) determines the resolution and light-gathering ability of the objective lens. Mathematically, the NA is expressed by the relationship:

$$N.A. = n * \sin \theta_o \quad \dots(2.6)$$

Where n , is the refractive index of the medium between the lens and the sample, and θ_o represents half the angle subtended by the lens at its focus (figure 2.2).

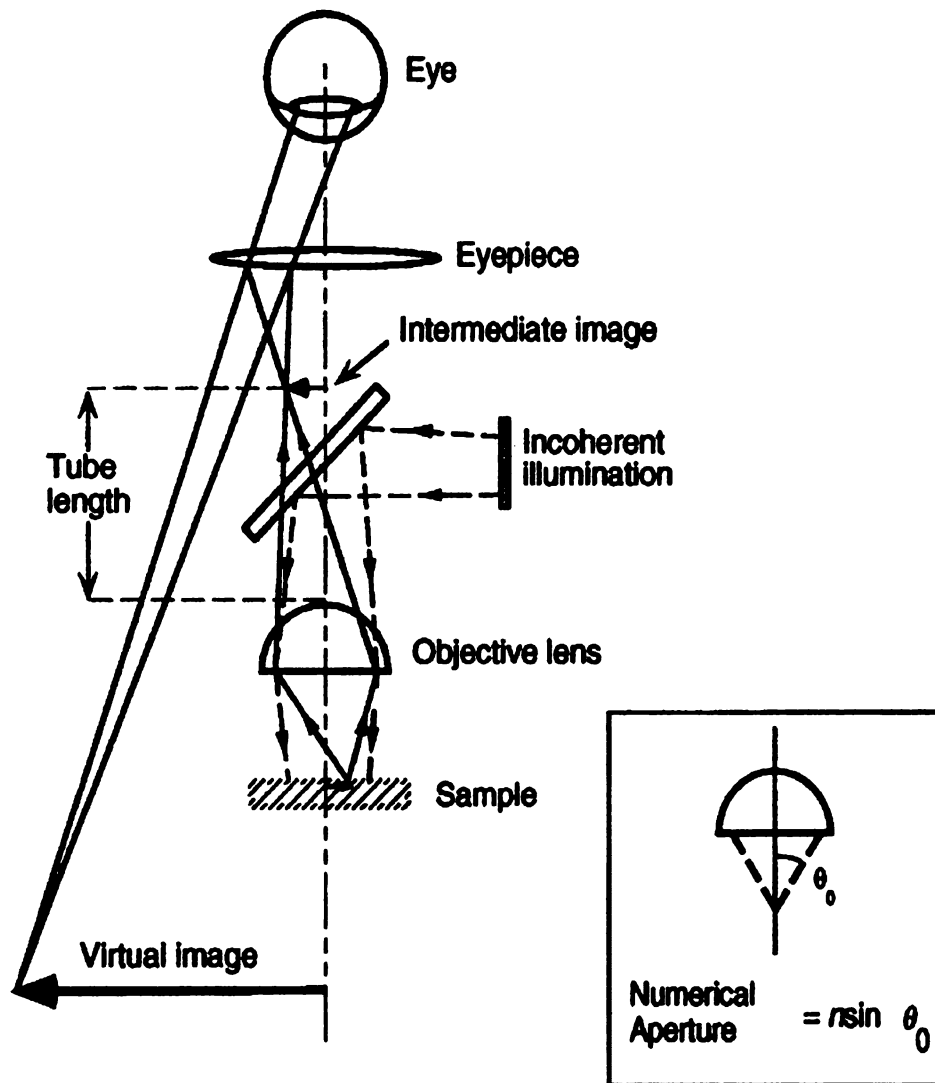


Figure 2.2 Simplified schematic of a conventional light microscope [21]

2.1.5 Objective Lens, focal plane, and depth of field

The objective lens is the most fundamental component for a light microscope. A basic understanding of it can be of capital importance to comprehend the way a CLSM works. In figure 2.3 a scheme of the front of an objective lens and the

entities it defines. First, we have the focal plane, defined as the region in which the parts of the sample appear sharp and distinct, “on focus” [23]. This region can be imagined as a finite slab perpendicular to the axis of the objective. Second, we can differentiate the focal distance as the distance between the objective front lens and the top of the focal plane. Finally, the thickness of the focal plane is defined as the depth of field.

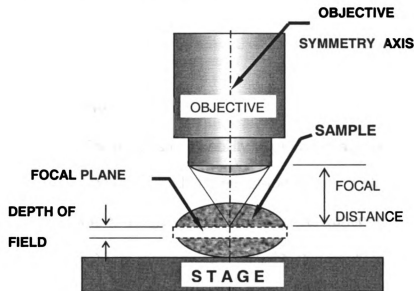


Figure 2.3 Illustration of the objective lens and the focal plane

2.2 CONFOCAL LASER SCANNING MICROSCOPY (CLSM)

The major advantage of the CLSM over a conventional light microscope is that, only light coming from the focal plane is detected, whereas light coming from the focal plane (out-of-focus light) is blocked. This is the origin of what is called an optical slice, which brings considerable improvement in the resolution respect to the conventional microscope. The improvement comes as a result of blocking the out-of-focus light, which causes the image blurring in conventional microscopy. In

the research field, confocal microscopy is known to be a valuable tool for obtaining high-resolution images and 3-D reconstructions of a variety of biological as well as material science specimens [25]. The Laser Scanning Confocal Microscope (CLSM) uses a laser beam as an illuminating source. This laser beam scans across the specimen by means of an x-y mechanism. With the confocal principle an image of a specific plane of the sample can be produced. This is the fundamental difference between a conventional light microscope and a confocal one.

2.2.1 The confocal principle

The power of the CLSM resides in its ability to get an image only from the light in the focal plane. This means that all the out-of-focus light is blocked from the final image allowing a sharper image compared to the conventional light microscope. This feature is achieved by positioning a detector pinhole in light path. Light that is exclusively coming from the focal plane is focused at a point right in the position of the pinhole (figure 2.4). Thus, the pinhole only allows the light coming from the focal plane to go through directly to a detector on the other side of the pinhole. Light rays originally coming from out-of-focus regions have a focal point either in front or behind the pinhole, therefore, few of these rays make their way through the pinhole. As a consequence, the image is formed mostly by rays coming from the region of the sample located in the focal plane. This process provided the birth to the concept of optical section. An optical section can be better understood as a slice of the sample coinciding with the focal plane level. The advantage is that an actual sectioning was not necessary to perform, the

sample remains intact and repetition of the process can be done. Once light of the region not in focus has been discarded in the final image, resolution and contrast are drastically improved respect to the conventional light microscopes.

Figure 2.4 shows the confocal principle while figure .2.5 shows a typical CLSM system.

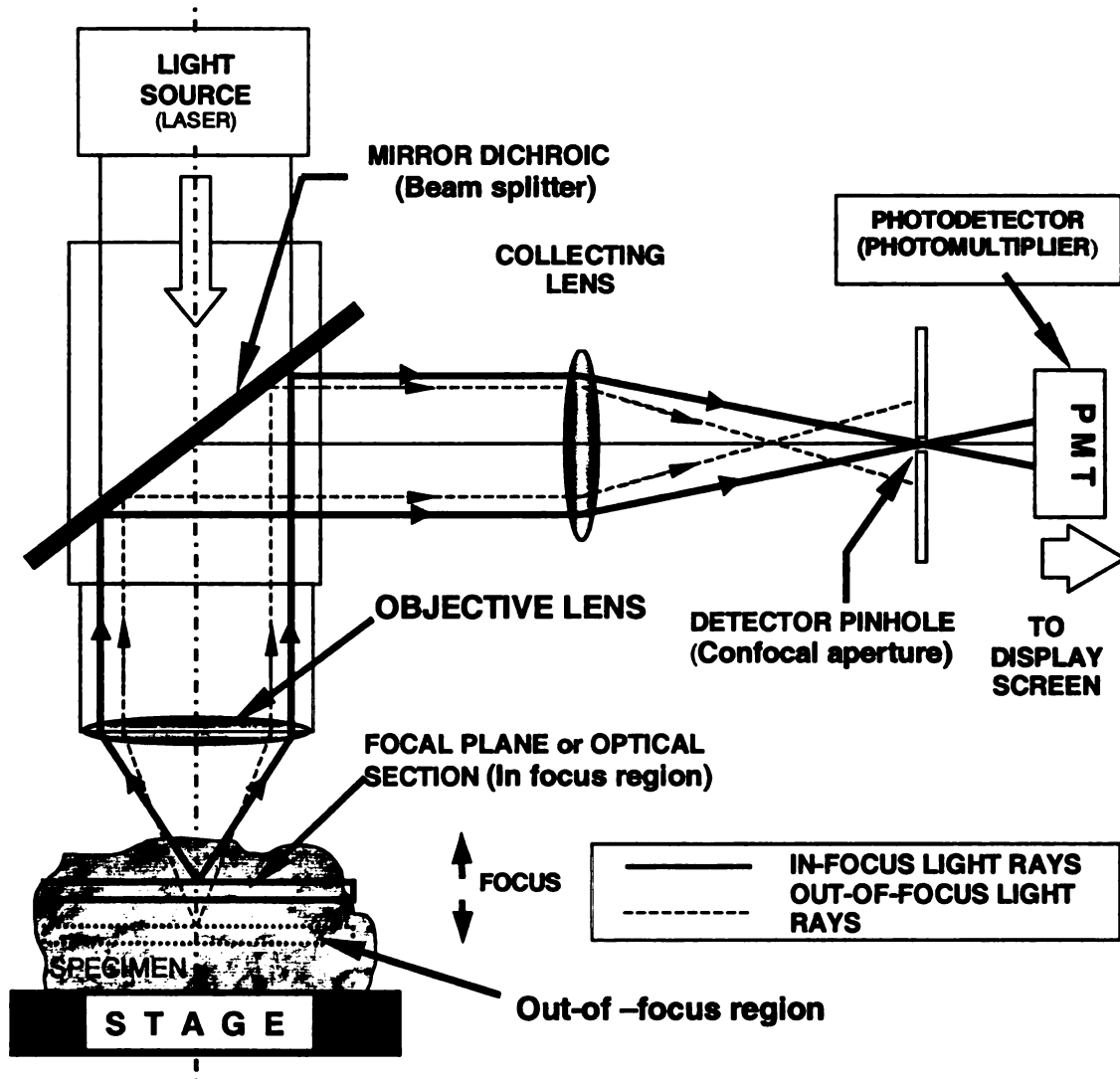


Figure 2.4 The confocal principle

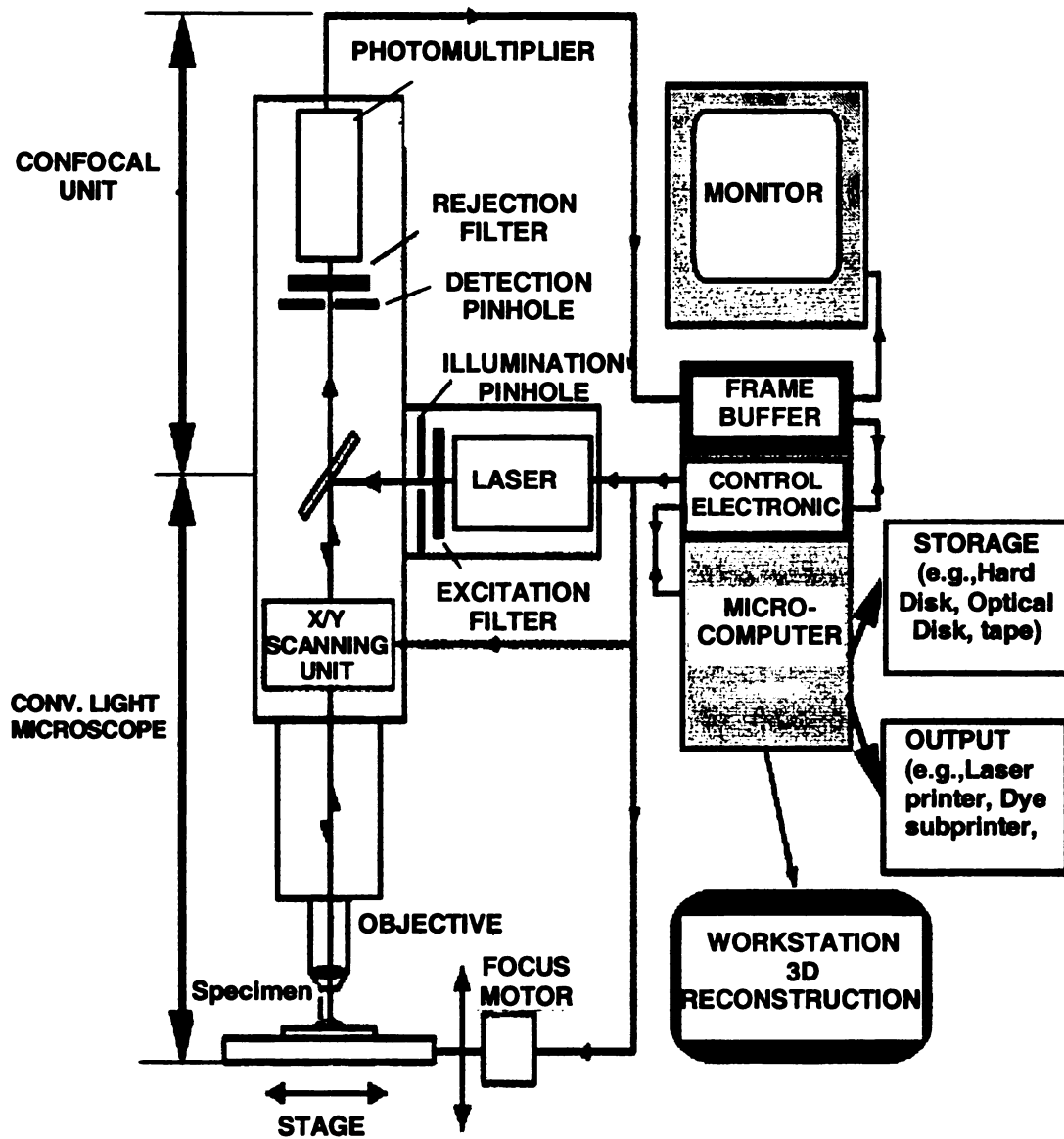


Figure 2.5 A typical Laser Scanning Confocal system [25]

2.2.2 Operations in the CLSM

Most operations in the CLSM can be achieved due to the motorized stage and the x-y movement of the laser beam. The motorized stage is usually able to move axially (z) with its position controlled by the microscope software. Some models also allow the stage to move in the transverse direction (x-y), this feature could be use to artificially increase the FOV and consequently the sampling area.

2.2.2.1 Z-series

The optical sections collected through a specimen conform a series of 2D grayscale images that are the usual data a CLSM can provide. This optical sections series are referred as Z-stack (figure 2.6). The optical slices in this z-tack could be electronically overlaid to produce an extended focus image, or the signal intensity information can be manipulated to produce a 3D display (topography).

When overlaying the optical slices, the user must decide beforehand the size of the image to be obtained, the number of optical sections and the vertical distance between two consecutive optical sections (Z-step size). The relevance of these three factors in the 3D size of the z-stack not only is related to storage space and availability, but also has subtle effects over the processing, display and control of this data [25]. Z-step size selection is a critical issue that includes the thickness of the sample to be imaged, the focusing movement and the resolving power of the objective lens. Here, the fineness of the stage movement is of capital importance, as this will dictate the lower limit for the z-step.

2.2.2.2 Phi -Z Sectioning

A phi-z section is an optical section taken in the vertical plane (parallel to the optical axis) rather than in the usual horizontal plane. To accomplish this in a CLSM, the beam is scanned repeatedly across a single line defined by the operator. Each scan will take place at a level deeper than the previous one until the total depth is reached. The total depth of the phi-z section depends on the on-screen magnification, whereas its thickness depends on the size of the laser spot (figure 2.7), which is in turn controlled by the NA of the objective.

2.2.2.3 3D reconstruction (Topography)

3D-reconstruction is most complex among the LSM's special features, which allows to obtain the surface topography for materials science samples and signal intensity variations in the case biological-fluorescent images.

The results of a z-series are the intensity as a function of pixel position (x,y) and slice depth (z), i.e. $I(x,y,z)$. For each pixel position (x,y), intensity is also a function

The intensity normally peaks at the surface. In figure 2.8 the intensity profile is represented over z at three points (x₁, x₂, x₃) on a step-shaped surface. The positions of maximum intensity (Z_m) of these curves, corresponds to the z value of the surface at this pixel location. As the intensity curve can vary with geometry and material of the specimen, the software usually offers three methods of determining the z value for the surface. By determining the coordinate of:

i) Z_{sp} the gravitational center of the curve $I(x_0, y_0, z)$

ii) Z_{max} the maximum of the curve $I(x_0, y_0, z)$

iii) $Z_{1,max}$ the first maximum of the curve $I(x_0, y_0, z)$

Mostly, the values obtained with the three methods will be very close, as in figure 2.9(a), where $z_{sp} = z_{max} = z_{1,max}$. Sometimes the results can differ greatly as it is the case in figure 2.9(b). The functions contained in the topography software allow to obtain a z surface coordinate for each pixel (x,y), which is in most cases a good representation of the specimen surface. This is stored in a matrix called the z-matrix (z(x,y)). Additionally, the intensity maxima at each (x,y) pixel is calculated and stored in the intensity matrix I(x,y).

Different types of rendering are available in addition to the topographic view itself. Z-maps, contour lines (isolines), relief images, volume determinations, statistical parameters (height and gradient histograms), and roughness parameters such as transition profile (tp), maximum peak to valley height (Ra), and average height (Zm) are possible with the confocal software [23]. Figure 2.10 shows a simple schematic showing the way in which topography is rendered. 3D reconstructions are obtained using the information stored during the gathering of the Z-stack.

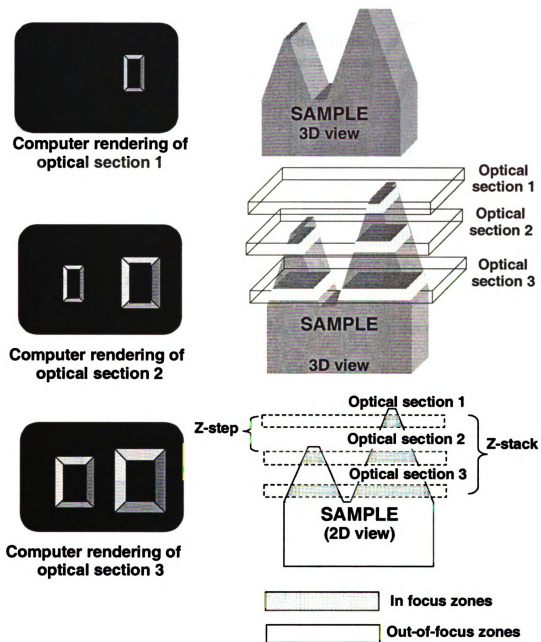


Figure 2.6 Z-stack computer rendering of a simplified sample

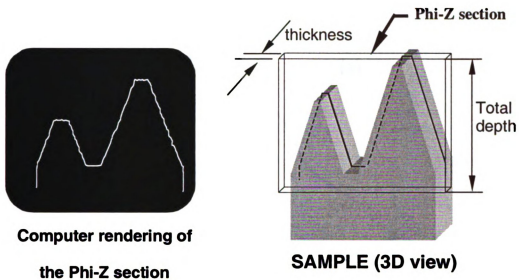


Figure 2.7 Simplified schematic of a phi-z section

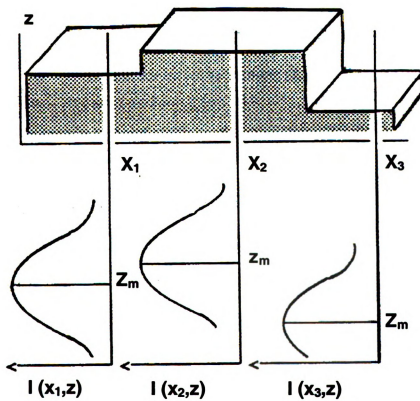


Figure 2.8 Intensity profiles and its relation to surface position

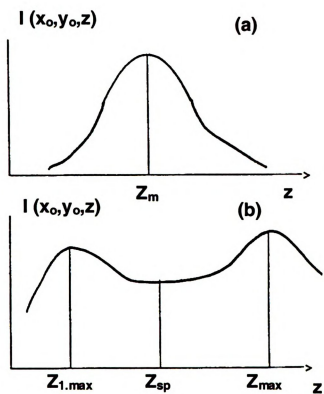


Figure 2.9 Intensity profiles shapes

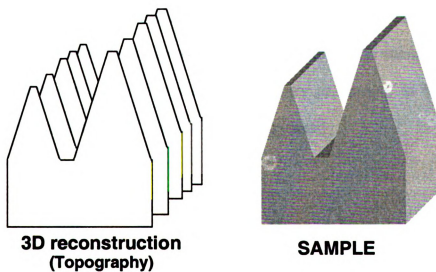


Figure 2.10 Simplified rendering of a 3D reconstruction

2.3 THE SCANNING ELECTRON MICROSCOPE (SEM)

In this apparatus an object is scanned in high vacuum by a concentrated electron beam. The image is obtained out of the collection of secondary or backscattered electrons from the sample in the spot where the electron beam strikes. Because the number of collected electrons is dependent on the nature of the material and its geometry, images with excellent geometrical detail are acquired.

The SEM has a better transversal resolution than a CLSM for the diffraction wavelength of an electron beam is as small as 0.04 nm. In practice, however, the resolution of an SEM is diminished by aberrations caused by electron scattering and other artifacts. Practical SEM resolutions usually range from 3 to 6 nm [20].

Another advantage of the SEM is the possibility of attaching an energy dispersive x-ray spectroscopy system (EDS system). This powerful tool allocates for the chemical element identification and quantification.

Although SEM electron beams have extremely short wavelengths, the NA aperture is particularly small. This results in SEM images remaining in focus for a large range of working distances and permanent 3D appearance, which doesn't allow for depth information to be extracted. Furthermore, The vacuum needed for SEM operation makes this microscope extremely expensive. In figure 2.11 a schematic representation of a typical SEM is rendered.

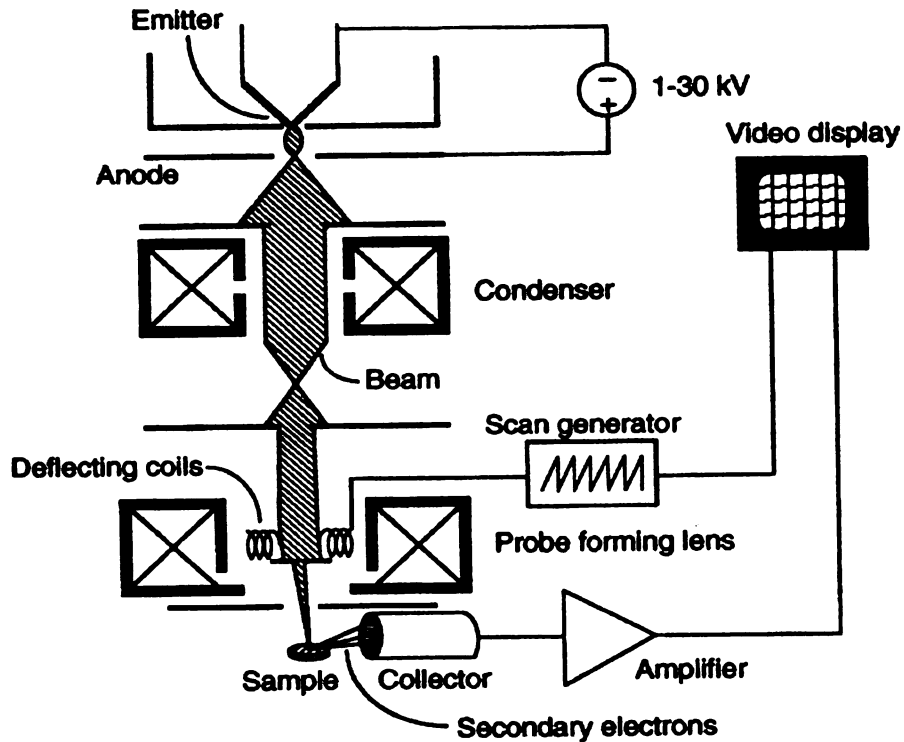


Figure 2.11 Simplified schematic of a SEM [21]

2.4 THE ATOMIC FORCE MICROSCOPE (AFM)

The principle of operation of an Atomic Force Microscope (AFM) consists of a fine ceramic or semiconductor tip scanning the surface of the sample, resembling the scanning of a needle in a phonograph (figure 2.12). The tip is located at the end of a cantilever beam, which deflects according to the force of interaction with the surface. This force is measured by the deflection of a light beam that is reflected from the upper side of the cantilever beam and impinging on a detector, which determines the position of the cantilever. There are two modes in which an AFM can operate depending on the way the tip interacts with the surface. If the

tip touches the surface during the whole scanning, the contact mode is being used, while in tapping mode tip only taps across the surface being tested.

A major advantage of the AFM is its usefulness when profiling a surface. The fact that the tip is actually “touching” the surface makes the AFM a very reliable and accurate tool for estimating the surface topography [21]. Typical transverse resolution for AFM falls within 0.1 nm and 1 μm , and depth resolution has an average value of 0.5 nm. Despite its high resolution the AFM has been proved to have some drawbacks due to the relatively slow scan, very small space of probe to sample, difficulty to use in deep holes, and easiness for a tip to be damaged.

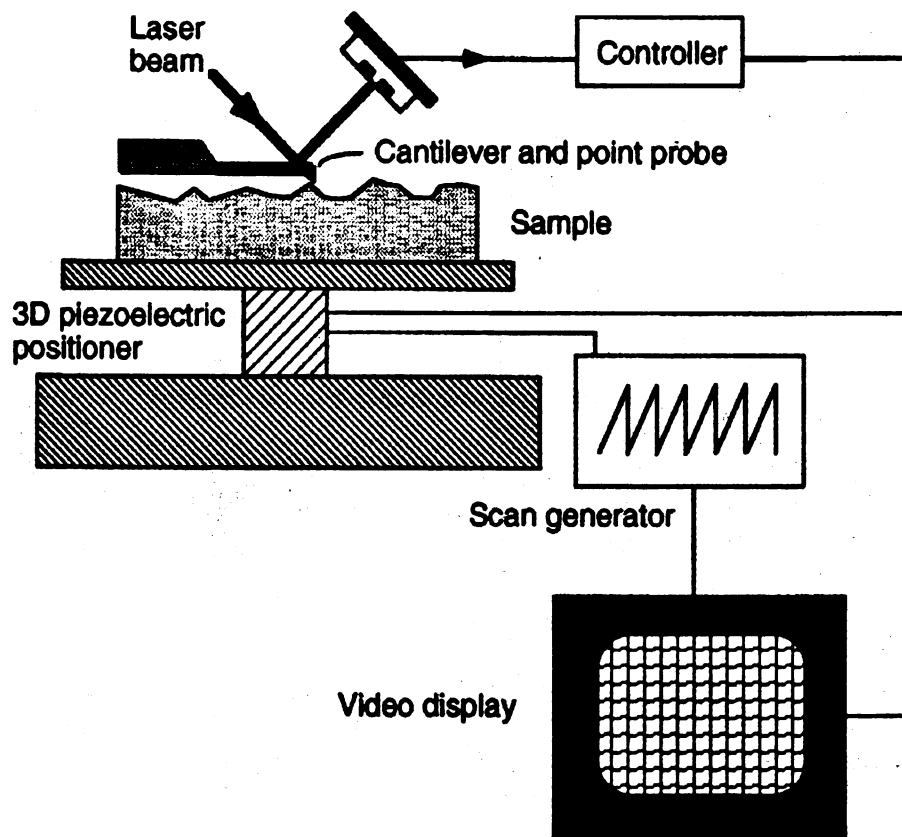


Figure 2.12 Schematic of the AFM principle of operation [21]

Chapter 3 : STATEMENT OF THE PROBLEM

3.1 LITERATURE REVIEW ON SURFACE TOPOGRAPHY

Surface evaluation, in particular surface topography, plays a prominent role in the analysis of wear because it supplies information about the local mechanisms that have been operating, their magnitude and their contribution to the overall wear rate [26]. In order to perform a micro level analysis of the wear in cutting inserts, an accurate 2D and 3D images as well as measurements are needed. These images and measurements should be able to show how the wear evolves to delineate local information on wear.

So far, the traditional methods used to quantify tool wear have included reflected light interference microscopy [27], scanning electron microscopy, and stereo microscopy. But due to the limitation on the depth of field, the difficulty while obtaining and interpreting images, and the high cost involved, [28] these methods have proven to be burdensome and time-consuming [26]. Also, conventional methods of surface measurement have involved stylus profilometers. However, this method has a number of disadvantages such as the limitations on the detail they can resolve, the slow scanning rate, and the potential damage to the surface investigated. Additionally, when using stylus profilometers, severe difficulties arise for the gathering of 3D data sets from surfaces [28].

Confocal laser scanning microscopy (CLSM) and its variants arise as an exciting new development in the field of microscopy with the potential to revolutionize surface analysis. Among the capabilities of CLSM are the fast and convenient recording of surface features and the determination and analysis of the true

surface topography. These capabilities provide the unique characteristics of the CLSM such as increased depth of field, minimal sample preparation, and adequate image quality for engineering purposes, and savings in costs relative to SEM technology. Further, CLSM measurement technology facilitates the use of new surface parameters that add to the traditional ones [28].

3.2 LITERATURE REVIEW ON CLSM APPLICATIONS

Since the commercial introduction of the CLSM in the early 80's, this microscope has been established as a powerful tool in biological and medical sciences. However, its use in tribological and metallurgical fields has been exceedingly limited [29]. Reflection CLSM, as stated by Wessel et al [30] is an underestimated quantitative, topographic imaging tool and a real alternative compared to SEM and AFM

During the past few years some comparative studies on the performance of traditional methods versus CLSM have been carried out in wear measurement, tribology, fractography, and biomedical sciences.

Anamalay et al, [28] compared surface parameters of three surfaces with different machining finish using CLSM techniques and conventional profilometer methods. They concluded that the use of a CLSM helps to avoid the profilometer's limitations of accuracy that originate from the size of the stylus. Such limitations are not found in a CLSM as long as objective lenses with suitable NA's are used.

In their tribological research of rolling-sliding wear surfaces of cast iron, Hanlon et al. [29] found a very good agreement between the results obtained by a CLSM and by an AFM, when profiling the worn surfaces. This implies that the CLSM technology provides an accurate reproduction of the surface geometry. The correction for tilting and the elimination of signal noise were the core part of the data post processing in this study.

Gee and McCormick [26] used a Confocal Scanning Microscope (COM) for the examination of worn alumina (Al_2O_3) surfaces. In this study, a previous comparison between profiles made by a diamond stylus profile and a COM on a glass was performed. The COM profiles presented a better response than the profile measurements system. Besides that, the COM proved to give better contrast than conventional optical microscopes for the alumina specimen, and to be particularly useful for the measurement of the topography of the alumina wear surfaces.

Wessel et al, [30] made a comparative work on the imaging of human hair and concluded that the precision of a reflection CLSM profile measurement of small structures depends much on the geometry and the optical properties of the investigated object. In addition, they suggested that for a good validation of height resolution the use of an AFM was essential.

3.3 RESEARCH FOCUS

Most of the work published regarding 3D tool wear characterization is related to the traditional methods of white light interferometry [27,31] or contact profilometry

[32]. Publications on tool wear (crater and flank wear) being analyzed with CLSM are rarely found. This is especially true when it comes to single and multi-layer coated carbides.

The difference in optical properties between coatings and substrate and the lack of previous CLSM-based works, make the CLSM wear imaging very challenging. On the other hand, the desirable capabilities of CLSM for profiling, height discrimination, and 3D-topographical reconstruction represent a real possibility for accurate tool wear characterization.

The focus of this study is to obtain a confocal 3D (topographical representation of the wear evolution of multi-layer cutting inserts, as well as the confocal profiles in specific locations .The measure of wear descriptors is also considered.

Chapter 4 : EXPERIMENTAL WORK

4.1 MACHINING EXPERIMENTS

The experimental work was performed at the Physics Shop facility of the Biomedical Physical Sciences Building at Michigan State University. The machine used was 8033 Clausing /Colchester lathe (figure. 4.1). This lathe allows for cutting speed to be set and programmable feed and depth of cut. This lathe was well suited for the experiments since the revolutions per minute (RPM) could be controlled in order to maintain the cutting speed constant.

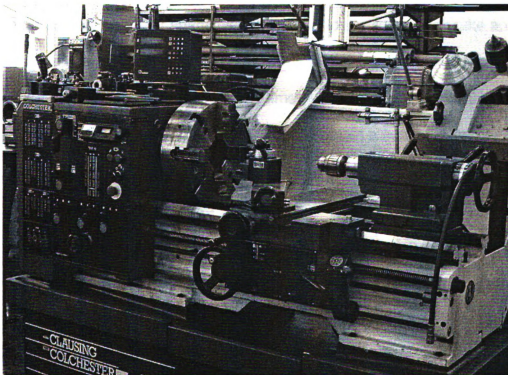


Figure 4.1 Clausing/Colchester variable speed lathe(Model 8033)

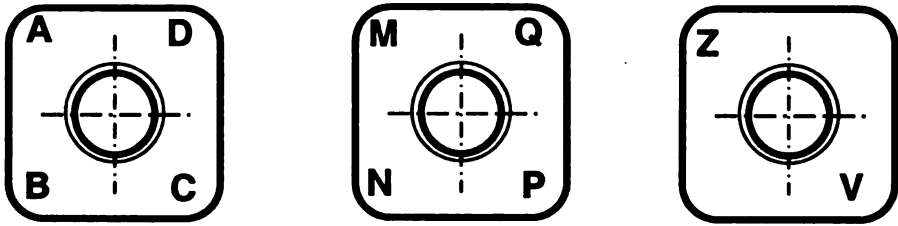
4.1.1 Machining conditions

The experiments were run in dry at the constant feed of 0.3175 mm/ rev (0.0125 inch/rev), depth of cut of 1.905 mm (0.075 inch), cutting speed of 250 m/min (820 sfpm). This cutting speed was specifically chosen following three criteria: The range of optimal speeds provided by the insert manufacturer's, the need for obtaining as much measurable wear as possible in the shortest time, and the torque limits of the lathe. Similarly, the feed and depth were selected following manufacturer's suggestions. In addition other aspects of the experiment were also considered, which are minimal chattering, good surface finishing and optimal area size for imaging. After few trial runs the approach angle was set to 5 degrees and the tool-holder shank was machined to provide a back rake angle of 2°. These angles set a compromise between minimal chattering and proximity to orthogonal cutting conditions. Machining times were interrupted at: 60 s, 120 s, 180 s, 240 s, 300 s, 480 s and 720 s. in order to obtain a cutting edge at each of these times. Thus, allowing for the wear evolution to be observed as a function of time. Table employed 4.1 shows the corners and inserts in relation with the machining time. The alternation in the corners was designed in order to avoid the temperature influence over the results when machining corners of the same insert consecutively. The corners with machining times of 10 s and 30 s were discarded because the wear on them was not measurable with the confocal microscope.

4.1.2 Work material

Steel rounded bars of AISI 1045 steel were purchased from ALRO Steel, Inc., Lansing, MI, and used as work material. The size of the bar stocks were of 6" diameter and 18" length.

Table 4-1 Inserts and corners used in the experiments

		
INSERT NUMBER	CORNER	MACHINING TIME
1	A	480 s (failed)
2	M	300 s
1	B	240 s
2	N	180 s
1	C	120 s
2	P	60 s
1	D	30 s (discarded)
2	Q	10 s (discarded)
3	Z	480 s
3	V	720 s

4.1.3 Inserts and toolholder used in the experiments

The inserts for the experiments were provided by Kennametal, Inc., Latrobe, PA, and had a SNMA 190612 ISO designation (ANSI Catalog # SNMA643). The toolholder was purchased from Production Tool Supply, Lansing, MI; and had the designation MSRRNR16-6D. Figure 4.2 displays the mounting of the insert, toolholder and chipbreaker. Figure 4.3 shows the insert geometry as provided by Kennametal.

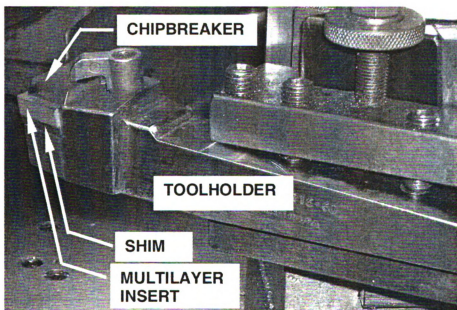


Figure 4.2 Insert and toolholder arrangement

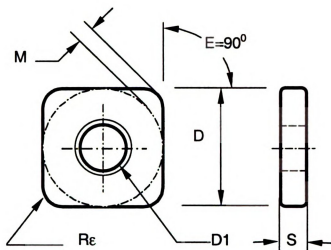


Figure 4.3 Geometry of a the SNMA 643 insert [35]

Table 4-2 Geometrical dimensions of the SNMA 643 insert [35]

SNMA 643 DIMENSIONS		
Description	ISO Catalog #	ANSI Catalog #
Unit of tool	Metric	Inch
aN M	0.000	0.000
aN	0.000	0.000
D1	7.930	0.3125
D	19.050	0.7500
E	90.000	90.000
L10	19.050	0.7500
M	3.452	0.1359
Rε	1.200	0.046875
S	6.350	0.25

4.1.4 Coating materials and substrate

The multi-layer insert was provided by Kennametal as a KC9315 grade insert. The top layer was made of Titanium Nitride (TiN), followed by the layer of Aluminum oxide (Al_2O_3), which in turn was above the Titanium carbonitride (TiCN) layer. As technical information on thickness of layers was not provided, a section of the insert was obtained using an Electrical Discharge Machine (EDS) and the thickness of each layer was obtained using a Zeiss LSM 210 confocal microscope in reflective mode (figure 4.4). TiN thickness was found to be $2.5\ \mu\text{m}$, Al_2O_3 $7.1\ \mu\text{m}$, and TiCN $7.8\ \mu\text{m}$. The substrate was C6 grade cemented carbide.

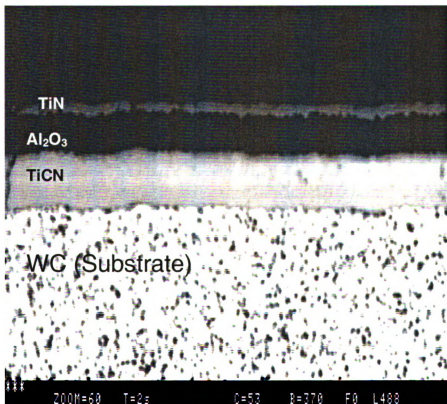


Figure 4.4 Reflection confocal image of the multi-layer insert cross section

4.2 CONFOCAL MICROSCOPY DATA ACQUISITION

Confocal microscopy data acquisition was done on a Zeiss LSM 210 (figure 4.5) at the Center for Advanced Microscopy at Michigan State University

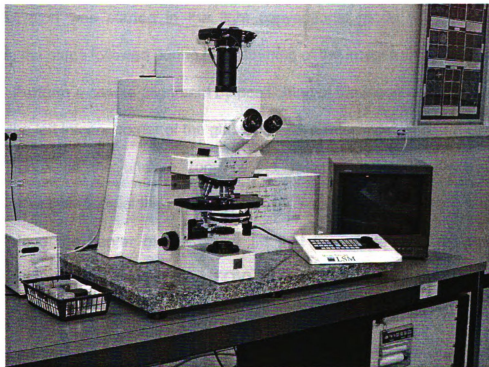


Figure 4.5 Zeiss LSM 210 confocal microscope

The following are the procedures and methodologies used for the confocal images. As a general rule, before starting the final gathering in each mode, many attempts were performed to optimize the acquisition parameters for the insert materials.

4.2.1 Crater 2D images

2D images were obtained in reflective mode using the Zeiss LSM 210 confocal microscope. The laser line used was the Argon-488 laser (L488 in micrographs legend bar) at 100% power. A 5X objective and a default screen zoom of 20 were selected, for convenience in capturing the whole area of the crater. Provided that each session was started in the light conventional mode with focusing the oculars, the steps followed during the gathering of the images were as follows:

- Perform a coarse alignment by positioning of the insert on the stage using the left inferior corner of the glass slide as a reference.
- Focus on the unworn zone of the specimen using the conventional reflective mode of the microscope.
- Move the center of the ocular so that the whole worn zone can be captured in the field of view (FOV).
- Change to confocal reflective mode and optimize the contrast and brightness with the color range indicator. During the optimization of parameters, it was found that keeping the brightness fixed at 400 (B=400), the contrast for optimal image ranged within C=40 to C=62.
- Proceed with the fine alignment. The distance function of the measure menu in the microscope software was used to define horizontal and vertical references for the edges of the insert. Figure 4.6 shows the position and values of these references.

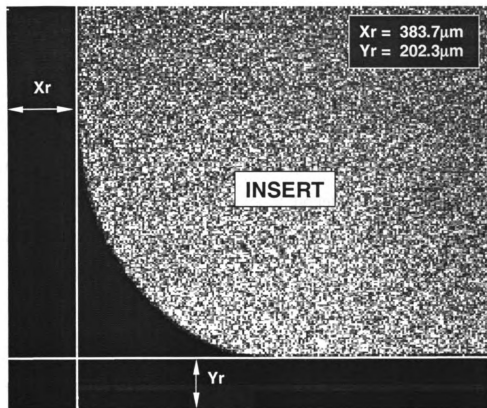


Figure 4.6 References for alignment in the LSM 210 pictures

- Store the image in the LSM 210 hard disk in PIC format.
- Transfer of files to a LSM 310 software for file format conversion (PIC to TIFF format) of the pictures files. PIC files cannot be read by most of the image processing software, while TIFF files can be easily recognized by most imaging software.

4.2.2 Topographical 3D images of crater wear

Crater wear topographical images of all the corners were obtained by means of the advanced three-dimensional reconstruction feature provided in the LSM210 software. The optimization of parameters for this part involved multiple trials with the four different lasers (He-Ne $\lambda = 633\text{nm}$, Argon $\lambda = 488\text{-}514\text{ nm}$, Argon $\lambda = 488$,

and Argon $\lambda = 514$) proofs with the digital filters (lowpass and highpass filters), z-step values , and number of sections involved. Optimal parameters for the topographical images were set as follows: 5X objective, L488 (Argon) laser line at 100% of the power (F0), contrast of 150, brightness of 405, z-step value of 49700nm, and 22 optical sections. Due to the difference in optical properties of the tool materials, the gravitational center of the intensity curve was chosen as the method for determining the z surface coordinates. Then, the LSM 210 software produced a z surface coordinate for x,y each pixel, that is , the z- (x,y) matrix.

The sequence of steps for the gathering was identical to that used for the 2D images in section 4.2.1 until reaching the fine alignment step. After that, the topography reconstruction required its own steps:

- Change contrast and brightness to 150 and 405
- Follow the sequence of buttons needed for surface reconstruction.
- Store the z-matrix in the hard disk (TOP format file)
- Transfer of the z-matrix to the LSM 310 software for post-processing and conversion of the TOP files to TIFF format.
- First post-processing to obtain: two 3D views (left and front orientation) and isolines view. For this post processing the optimal parameters were found to be: Height: 62, Lowpass filter (Kernel=1), and $D/\mu\text{m}=60-80$ (Isolines function).
- Store the 3D views and isolines in a TIFF format

- Editing and 2nd post-processing in Adobe Photoshop 7.0 to obtain the final 3D topographical views.

The shape of the crater wear was verified in the early stages of the research using a replica of a worn corner. This corner was previously used to machine a 1045 steel at 660 sfpm, 0.356 mm/rev feed and 1.905 mm depth of cut. Vinyl Poxysiloxane, an impression material used in dental care, was used to make the replica. Before doing the imaging in the LSM 210, the replica was coated with gold to assure uniform optical properties in the worn area.

4.2.3 Maximum crater depth values and locations

The determination of the maximum depth location in each corner was a crucial task. For one thing, the time evolution series for crater and flank wear were done in the maximum depth locations. Due to this relevance and the limitations of the microscope software to provide for an automated method, the search for the maximum depth in each corner was done using three different methods.

Visual inspection method

The visual inspection method consists of finding the darkest point in the crater through visual inspection of the 2D confocal image of the corner and defining its location respect to the edges of the insert. This method is fast to perform and is based on the common optical idea that deeper points correspond to darker points. However, this method has consistency problems as human error is definitely introduced.

Method of inspection using the Matlab Imaging tool

The semi-automatic method made possible to obtain a grayscale-value map of all the pixels in the image. The imaging tool of a Matlab 6.5 version was used to perform this task. The grayscale value (0-255) of any pixel in the image could be obtained just by positioning the cursor in a location. Once the pixel with the lowest gray scale value (maximum depth location) was found by inspection, the position of the pixel was defined respect to the edges of the tool. This method can diminish human error due to visual inspection because a numerical value (grayscale value) is used to find the darkest point.

Five-sections method

In the aim of automating and improving consistency, a search technique was outlined. This technique consisted in obtaining five equally spaced orthogonal sections out of the area that contained the maximum depth location. Then, the section that possessed the maximum crater depth was selected as the possible maximum-depth section. This method was used for the left-view and front view orientations. Figures 4.7a and 4.7b illustrate the method.

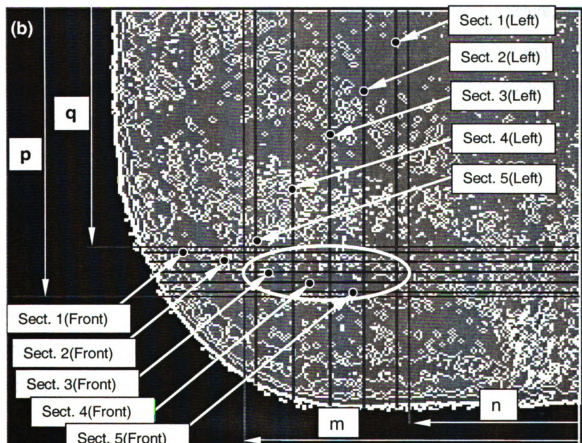
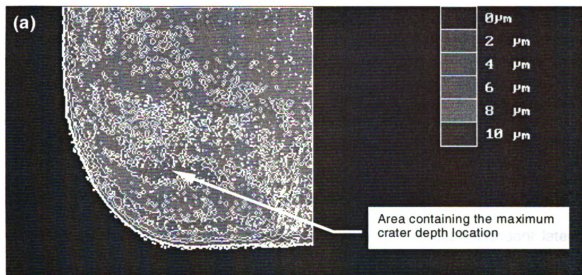


Figure 4.7 (a), (b) Five sections method (Isolines view)

The position of the orthogonal sections having a left view orientation (Figure 4.5), respect to the right side of the image was calculated using:

$$X_j = n + \frac{(m-n)}{50} [1+12X_i] \quad \dots (4.1)$$

Where:

m and n, are the maximum and minimum lateral limits of the area (μm), $(m-n)/50$ is the space between the last and first section and their correspondent lateral limits (μm), j is the section number in the image $j = 1, \dots, 5$, X_j is the position of the section measured in microns (μm) respect to the right side of the picture, and X_i is the auxiliar variable to add the distance between each section in the current area, $i = 0, \dots, 4$. The section number to pick from the associated topography file was determined by:

$$S_L = \frac{X_j}{11.453} \quad \dots (4.2)$$

where S_L is the section number in the left-oriented topography reconstruction and $11.453 \mu\text{m}$ is the distance between each section in the 3D topography software. In the same fashion the front-oriented orthogonal sections positions respect to the top edge of the image (Y_j), as well as the front section number in the 3D reconstruction (S_F), were found with:

$$Y_j = q + \frac{(p-q)}{50} [1+12Y_i] \quad \dots (4.3)$$

$$S_F = \frac{Y_j}{11.453} \quad \dots (4.4)$$

The references in this method were taken respect to edges of the image to match the way the LSM 310 software counts the sections in topography mode. However, the position of these sections can be readily converted to the references fixed in the edges of the tool (See 4.2.1).

Once the location of maximum depth was found in each method, the left view and front view sections associated with this location were extracted out the $z(x,y)$ matrix. Then, the measure function of the software was used to obtain the value of the maximum depth. Finally, an Excel data sheet was used to compare and obtain the maximum depth and its location out the several possibilities provided by the three methods for each machining time. From this point on, these locations and their correspondent depth values were regarded as the maximum-depth locations and maximum depth values.

4.2.3.1 Crater wear time evolution

The maximum crater depth locations (MCDL) of the corners with machining time of 300s, 480s and 720s (A-A, B-B, and C-C sections in figure 4.8) were chosen as references locations for time evolution analysis. All the sections passing through these three reference locations were obtained for all machine times. Then, these sections were overlaid using Adobe Photoshop 7.0 to finally give the crater evolution in time (Figure 4.9). **Images in this thesis are presented in color.**

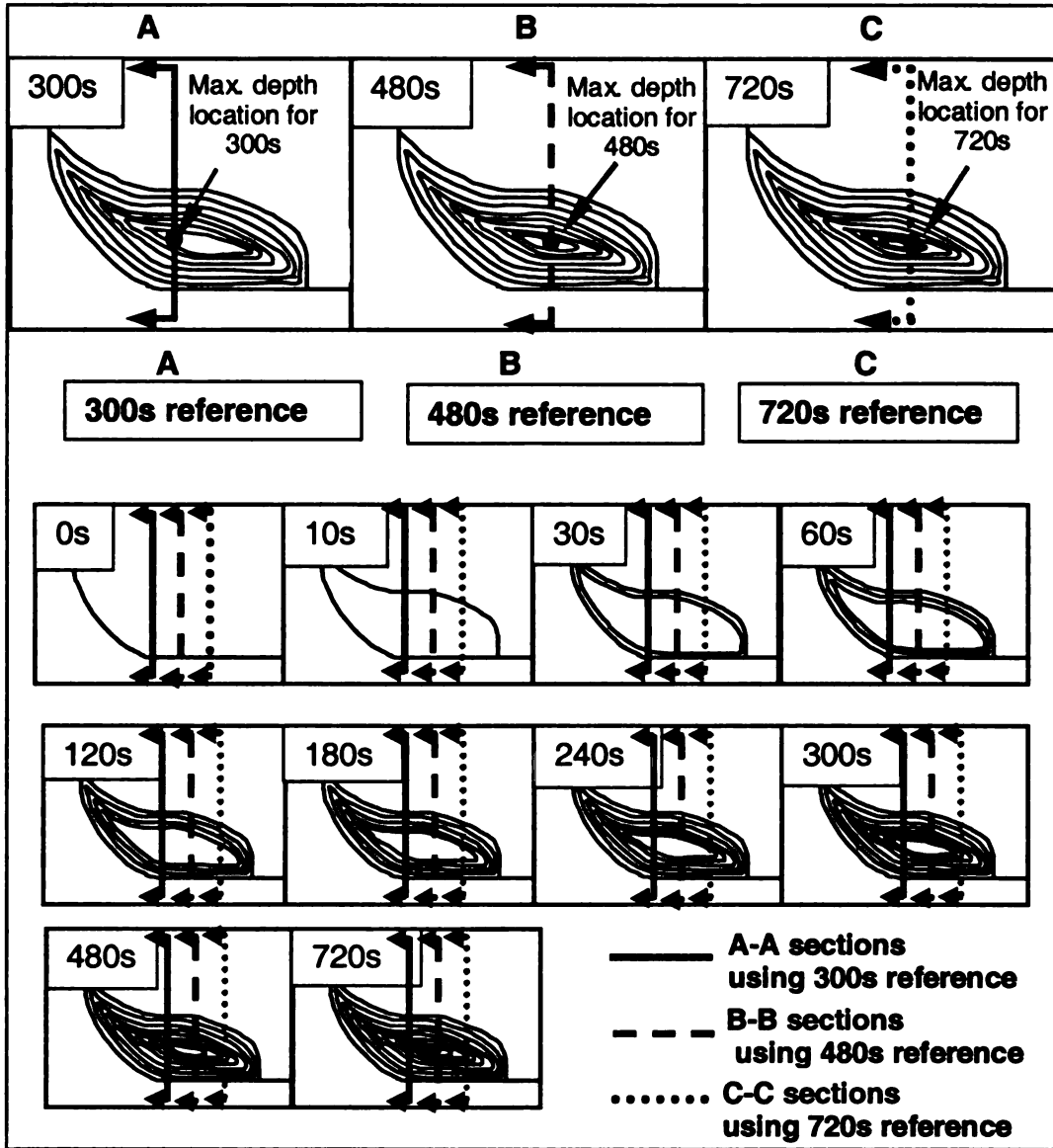


Figure 4.8 Reference locations for crater wear evolution

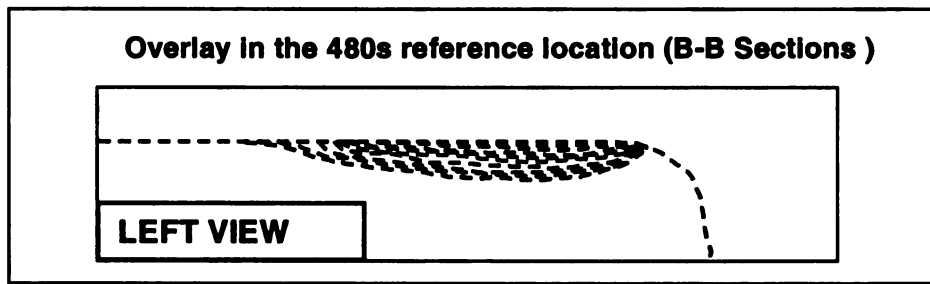


Figure 4.9 Evolution of the crater obtained overlaying the B-B sections

4.2.4 Crater wear Phi-Z sectioning

As three of the 22 optical sections of the z-stack were highly saturated ^(*), a validation of the values obtained with the 5X objective was needed. This was done using the phi-z function and a 50X objective, which has better transversal and depth resolution than the 5X objective. Using the phi-z function, right-view profiles showing the crater wear evolution at the MCDL's for 300s, 480s, and 720s were obtained. Optimization of the microscope parameters was also necessary resulting in the following settings: 50x objective, zoom screen of 20, 488 nm (Argon) laser line with 100% power, contrast: in the range of 53 to 75, brightness ranging from 400 to 414, z : xy ratio of 300% (ratio between the height and length of the display), 350 scan lines, and position: 50.

Measurements of maximum wear depth were carried out after the image processing. Images were overlaid and merged to increase the FOV of the 50 X objective and the relation between the pixel size and the distances was determined. These measures were done using the 50X objective resolution, and the pixel ratio changes when transferring the files from the LSM 210 computer to the computer that contains the LSM 310 software.

4.2.5 Phi-Z sections for flank wear

Phi-z sections of the flank face for all machining times were obtained for each corner. Again, the MDL's for 300s, 480s, and 720s (figure 4.9) were used as

^(*) A saturated image contains a great amount of saturated pixels .A pixel is saturated when its grayscale value is 255..

references. These phi-z sections had a right-view orientation and were used to show the flank-wear evolution in time. In this part, images were gathered with the same parameters mentioned in 4.2.4, except for, this time the z : xy ratio was 100%. The slope of the land wear was measured after the imaging post-processing for the different machining times. No 2D images or 3D reconstructions were acquired due to the limitations in the maximum displacement of the stage.

4.3 ELECTRON MICROSCOPY DATA ACQUISITION

Electron microscopy data acquisition was carried out in the premises of the Center for Advanced Microscopy (CAM) at Michigan State University. The SEM used was a JEOL JSM-6400 Scanning microscope (figure 4.9). The image acquisition for the SEM pictures was achieved with the SIS 3.0 (Soft Imaging System) software.

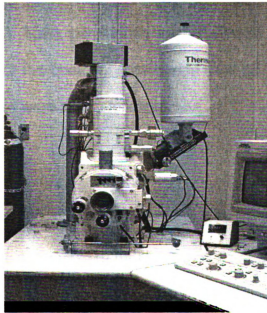


Figure 4.10 JSM-6400 Scanning Electron Microscope

4.3.1 Backscattered electrons (BSE) images

Crater wear

During the optimization of parameters for the data gathering in the confocal microscope, confirmation of the shape for the crater was needed. In the first stage of the optimization, confocal results showed that the crater had gone through the three layers and reached the WC substrate. Using the JEOL JSM-6400 Scanning microscope in backscattered electron (BSE) mode images of all corners were obtained. Backscattered electrons can be easily related to the Average atomic number of the material, and therefore used to build an “atomic number” image. In these images, zones containing chemical species of high atomic number will be seen brighter than those areas with chemical species of low atomic number. BSE images showed that during the cutting experiments only the first layer (TiN) had been worn out and that the Al₂O₃ layer was being exposed (Appendix C). Then, parameters were reviewed and adjusted to obtain the optimal settings for the confocal microscope data gathering. The acquisition parameters for this part were set as follows:

Accelerating voltage	25 KV,
condenser lens	9 (coarse) and 0 (fine)
working distance	15 mm
magnification	43X

Flank wear

Flank wear images were taken in BSE mode due to the difficulties that arose in the imaging with the LSM 210 (see 4.2.4). The information extracted out of these images made possible to differentiate the limits between the first two layers, and also helped to roughly interpret the phi-z profiles obtained with the CLSM microscope (Appendix G). The SEM parameters for flank wear images were set to:

Accelerating voltage	25 KV,
condenser lens	9 (coarse) and 90 (fine)
working distance	15 mm
magnification	40X and 250x

4.3.2 Energy Dispersive X-ray Spectroscopy and Dot maps

A spectral analysis of the chemical composition and distribution over the rake face was run using a Noran x-ray detector unit and EDS software (Vantage spectral 1.5.1). The specimen used for this purpose was the corner with the machining time of 300 s and the results can be seen in Appendix B. In addition, X-ray dot maps showing the presence of Ti, N, Al, O, and Fe in the tools were acquired for all machining times. The sequence obtained was to keep track of the growing crater area and the limits between the first and second layer. Also, line scans perpendicular to the trailing edge and parallel to the scoring marks were obtained while in the X-ray mode (Appendix D). The values for accelerating voltage and working distance remained unchanged respect to the values used for

BSE images, but the magnification was changed to 38X in order to allow for the EDS display to capture the area of interest. Also, the contrast and brightness had to be adjusted for a good image. The condenser lens was adjusted to 11 (coarse) and 40 (fine) to give an appropriate dead time during x-ray data acquisition. During the spectral analysis for the 300s corner the dead time fluctuated between 20 and 30 %, whereas during the dot maps acquisition it ranged from 30 to 40 %. The EDS time limit and dwell limit were set at 30 s and 25 ms respectively.

4.4 ATOMIC FORCE MICROSCOPY DATA ADQUISITION

The equipment used in this part of the research was the Nanoscope III Scanning Probe Microscope manufactured by Digital Instruments Inc., located in the Center for Advanced Microscopy at Michigan State University. The images were processed using the Nanoscope III version 4.23 rev. 6 software provided with the microscope (figure 4.11). The information obtained with this microscope constitutes the main validation of the data obtained with the: Zeiss LSM 210 Confocal Microscope. This validation was suggested in reference [30].

Because of the displacement limitations of the stage to obtain one profile of the insert, fourteen consecutive areas were scanned and their images merged using Adobe photoshop 7.0. These scans were performed in the corner with 300s of machining time, following a direction parallel to the trailing edge and passing through the maximum depth location. All the images were obtained using the J scanner tube, the nanoprobe NP silicone nitride tip, and with the DVM values set

to 7.89 volts and 2.72 volts, for the upper and lower position of the switch respectively. The acquisition parameters were set as follows:

Scan Controls

Scan size : 77.5 μm
 X offset : 0.00 nm
 Y offset : 0.00 nm
 Scan angle : 0.00 deg
 Scan rate : 4.07 Hz
 Number of samples : 512
 Slow scan axis : Enabled
 Z limit : 440 V

Channel 1

Data type : Height
 Z range : 2.50 μm
 Line directions : Trace
 Scan Line : Main
 (Disabled)
 Real time Plane fit : Line
 Offline plane fit : Full
 High pass filter : Off
 Lowpass filter : Off

Feedback controls

Integral gain : 3.00
 Proportional gain : 3.00
 Look ahead : 0.00
 Set point : 0.00 V
 Analog 1 : 0.00 mV
 Analog 2 : 0.00 mV

Other controls

Units : Metric
 Color table : 7
 Min. engage gain : 6.00
 Z modulation : Enable
 Tip serial number : (n/spec)

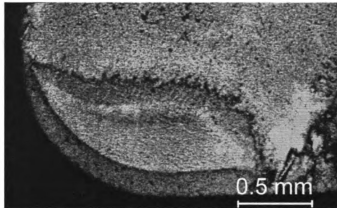


Figure 4.11 Nanoscope III scanning probe microscope

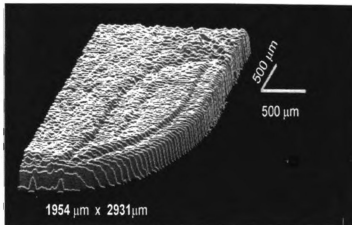
Chapter 5 : RESULTS AND DISCUSSIONS

5.1 VALIDATION OF THE CRATER SHAPE

The images obtained with the Vinyl Poxysiloxane replica and the SEM confirmed that the crater wear shapes obtained with the LSM 210 software were showing the real topography of the crater. Figures 5.1(a) and (b) show the 2D and 3D confocal views of a worn corner with a humped formation next to the trailing edge and, also the crater starting to develop on the other side of the formation.



(a) Confocal slice of the Vinyl poxysiloxane replica of a worn corner



(b) Topographical view of the Vinyl poxysiloxane replica of a worn corner

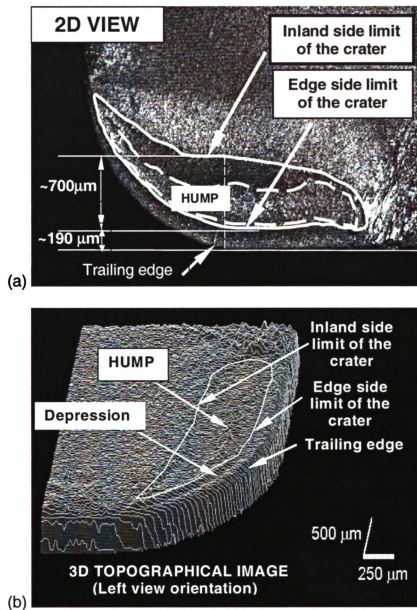
Figure 5.1 (a), (b) Confocal views of the Vinyl poxysiloxane replica

This validation weakened the idea about the difference in optical properties of the coatings playing a role on distorting the actual surface geometry. Similar information can be seen in appendix A the a corner machined for 300 seconds, which was imaged using the SEM microscope in secondary electron mode

5.2 CRATER WEAR EVOLUTION AND MEASUREMENTS

5.2.1 TIME SERIES OF CONFOCAL IMAGES

The 2D and 3D (topographical) confocal images exhibited particular features of the surface morphology. First, an unexpected hump that started approximately at 190 μm from the major cutting edge for all machining times except for the 720 seconds corner, in which the hump started at about 300 microns from the edge. Second, a thin depression preceding the hump of approximately 20 μm width, was observed at all machining times except for the 720 seconds corner. This was observed to act as boundary for the crater zone (edge side limit, figures 5.2(a) and (b)). Third, a crater zone that started at about 700 μm and grew with machining time towards the trailing edge was also found. Fourth, in the corner with 720s machining time a new humped island was observed next to the inland limit of the crater. The 2D shape and dimensions of the crater were observed to be approximately constant and delimited by the depression on the trailing edge side and the inland limit of the crater (Figures. 5.2 (a) and (b)).



Figures 5.2 (a),(b) Features of the crater wear for the multi-layer coated insert

Figure 5.3 shows the 2D evolution of crater wear using a slice on the brightest position and figure 5.4 renders the topographical (3D) evolution for all machining times. Both image sequences were obtained with the Zeiss LSM 210 confocal microscope.

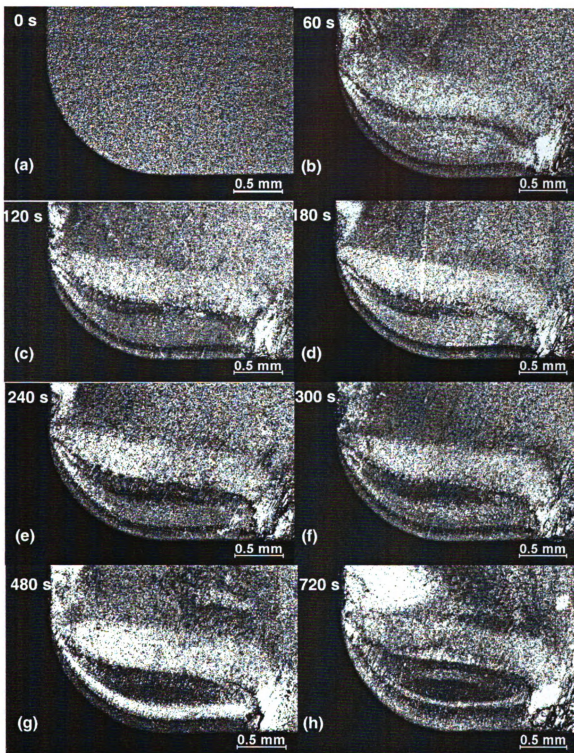


Figure 5.3 2D confocal images showing the evolution in time of the crater wear

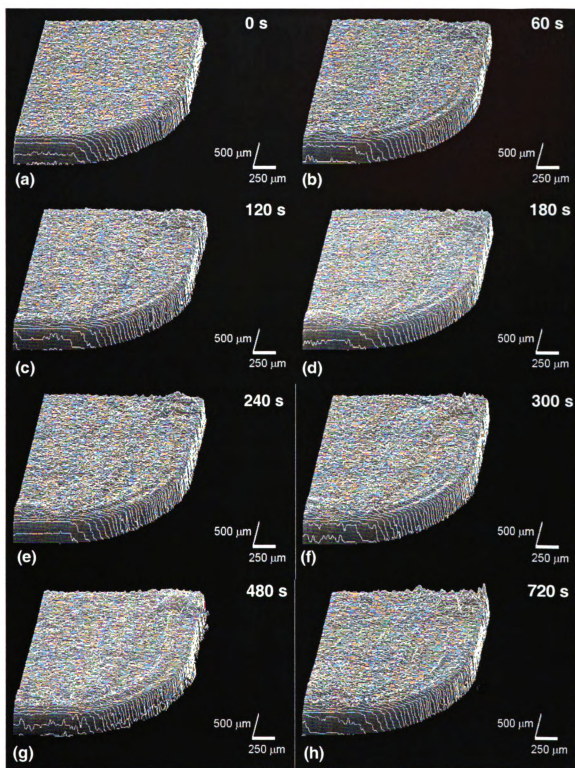


Figure 5.4 Topographical views of the worn corners for all machining times

5.2.1.1 BSE images and x-ray spectroscopy analysis of crater wear

BSE images revealed several details about the chemical composition of the different zones in the crater. For example, it was found that the crater zone, limited by the inland side and edge side boundaries, was composed of two main regions: a humped island made of TiN and a growing crater zone of Al₂O₃. Also, the thin depression observed in the topographical images turned out to include a very narrow zone of Al₂O₃. Further, traces of steel were found attached to the TiN coating specially in the limits of the crater zone (figure 5.5). In appendix B, the spectral chemical analysis and the x-ray dot map for the corner with 300s seconds machining time is shown. Appendix C shows the BSE images of the corners for all cutting times. Another interesting finding in the x-ray analysis was obtained with the linescan feature. The chemical analysis results showed that the linescan parallel to the chip flow (scoring marks) exhibited the Al₂ O₃ at the beginning of the TiN hump, whereas in the linescan perpendicular to the trailing edge Al₂O₃ was not detected. This trend was consistent throughout all the machining times and confirmed with the confocal microscope. Appendix D presents the linescans for a 300s machining times in both directions.

In the absence of a reliable and automated method for determining the limits between layers, the backscattered images were used to measure distances and areas of interest in crater wear. BSE images were able to provide different

brightness intensities for the areas of steel (AAN^(*)=25.8), TiN (AAN=14.5) and Al₂O₃ (AAN=10), thus, giving a means of differentiation between layers.

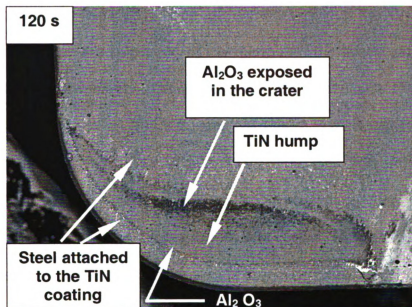


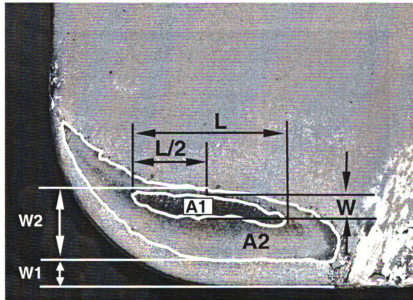
Figure 5.5 BSE image of a worn corner with the chemical elements observed

Two important areas were measured for all machining times. A1 was measured so that the darkest area (Al₂O₃) was enclosed and no TiN material included. A2 was defined as the crater area and its boundaries were delimited by the inland side and edge side limits (Table 5.3). The length (L) and the width (W) of area A1 were regarded as relevant as these values could provide information of the crater wear trend. A2 remained almost constant at around 84 000 μm² except for the value at 720s (75 000 μm² approximately). A1 exhibited a growing trend for all machining times (figure 5.6), with its width (W) and length (L) values also

(*) AAN=Average Atomic Number

increasing. However, the rate of increase was less pronounced for W than for L (figure 5.7), meaning that the crater in the Alumina zone (2nd layer) expands faster in length than in width. Three distances were also found to be of interest: the distance between the trailing edge and the beginning of the Tin hump (W1), the distance between the beginning of the hump and the inland side limit (W2), and the distance between the trailing edge and the inland side limit (W1+W2). The time-elapsing trends of W1, W2, and W3 (figure 5.8), suggested W1, W2, and W1+W2 remained constant at about 190, 500, and 700 μm respectively between 60 and 480s. The corner with 720s machining time presented a significant drop in W2 while increasing its W1 value. However, the value of W1+W2 was increased respect to the values observed between 60 and 480 s.

Table 5-1 Crater areas measurements for all machining times



Machining Time (sec)	L (μm)	W (μm)	W1 (μm)	W2 (μm)	A1 (μm ²)	A2 (μm ²)
60	371	17	174	498	6768	818048
120	844	74	188	472	40148	822385
180	1083	118	179	493	83760	831308
240	1141	188	202	519	157583	830021
300	1158	183	193	498	138980	845469
480	1858	306	179	516	439333	900182
720	1705	432.8	319	472	548853	749735

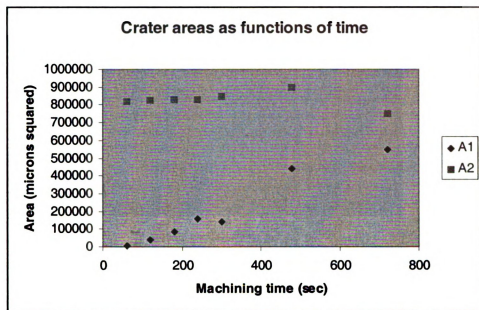


Figure 5.6 Plot of the crater areas evolution in machining time

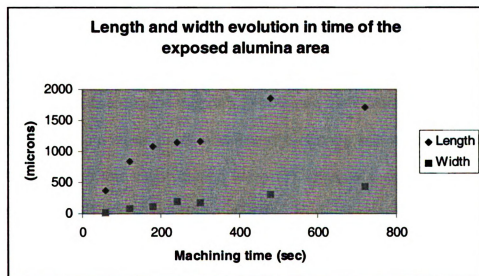


Figure 5.7 Plot of the length and width evolution for the exposed Alumina area

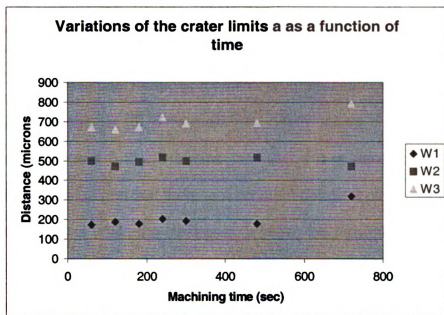


Figure 5.8 Variation of the width limits position of the crater in time

5.2.1.2 Maximum crater depth measurement

Maximum crater depth is accepted to give a clear idea about crater wear extent [3]; thus, any crater wear quantitative description should include it. The maximum crater depths and its locations (figure 5.9) obtained are enlisted in Table 5-1. The location of maximum crater depth was found to change with machining time. The position respect to the major cutting edge (Y) showed a consistent value that fluctuated between 500.1 and 683.4 microns, while the position with respect to the minor cutting edge (X) exhibited a wider range of variation (836.0 to 1248 microns). This implies that the peak interface temperature, which occurs in the vicinity of maximum crater depth [8], is changing its location as machining time increases. Additionally, the X value showed non-stable behavior between 60s

and 180s, then an approximately constant value between 240 and 480s, and finally a considerable rise at 720s (figure 5.10). These were interesting findings considering that traditional methods for crater wear measurement do not allocate for this type of behavior [6]. The maximum depth values evolved with a two-stepped shape (figure 5.11). It seems that 180 s is a transition point for the maximum depth value and that there is a constant behavior of the depth between 300 and 480s. In the latter, the closeness between the maximum depth value for 300 and 480s (2.3 microns) and the thickness of the first layer (TiN, 2.5 microns) could indicate the Alumina layer (second layer) was resisting the crater wear in such a way that stopped the crater depth growth. It is speculated also that because of this “barrier” effect, the crater wear is more evident in the TiN layer (top layer) during this period of time. The TiN humped area was decreased as the Al_2O_3 area (A1) expanded (figure 5.6). These findings seemed to be supported by the facts that the Alumina (Al_2O_3) possesses higher hot hardness and is also more chemical inert than TiN when machining medium-carbon steels [8], which means that Al_2O_3 is more likely to resist abrasion wear as well as diffusion and dissolution wear.

The validation of these depth values was done with a 50X objective for three machining times (300s, 480s, and 720s) and the results can be seen in Appendix E. A good agreement was found for the maximum depths corresponding to 300s and 480s, considering the increase and resolution when changing from 5X to 50X objective. However, there was a considerable difference when comparing the depth for the 720s machining time.

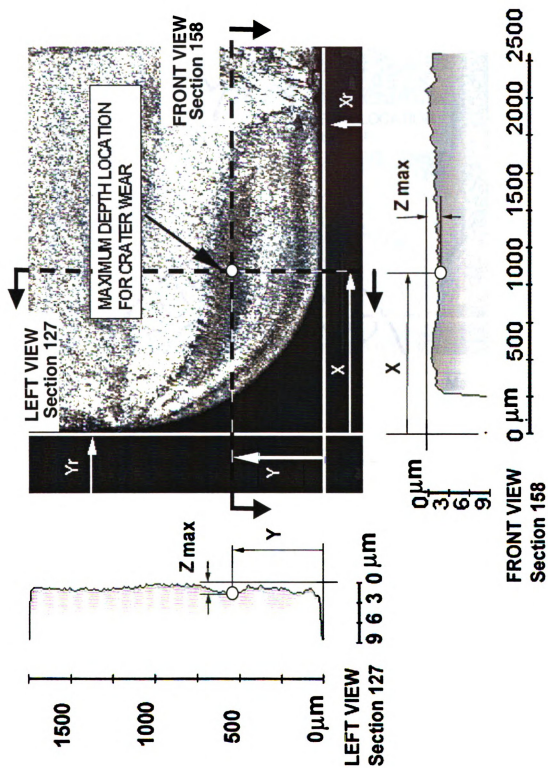
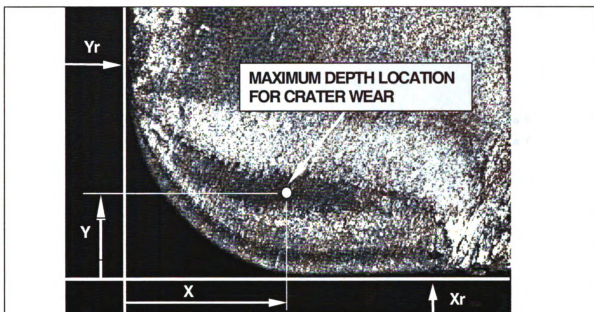


Figure 5.9 Orthogonal sections obtained at the maximum crater depth location

Table 5-2 Maximum crater depth location for all machining times



Machining Time (sec)	X (μm)	Y (μm)	Maximum Crater Depth, Z_{max} (μm)
60	755.8	683.4	1.7
120	1122.3	561.2	1.9
180	836.0	538.3	1.9
240	1088.0	538.3	2.2
300	1110.9	553.6	2.3
480	1099.4	500.1	2.3
720	1248.3	507.8	2.3

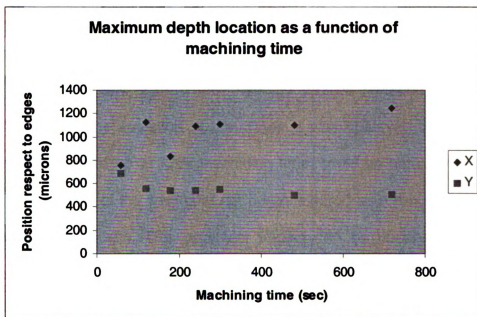


Figure 5.10 Plot of the maximum crater depth location versus machining time

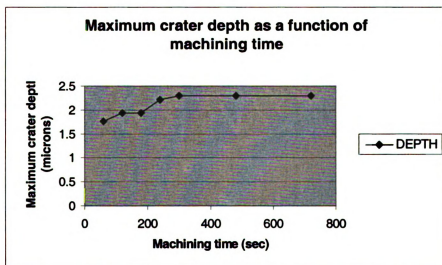


Figure 5.11 Plot of the maximum crater depth versus machining time

5.2.1.3 Time-evolution profiles for crater wear (Overlays)

The evolution in time using the 300s, 480s and 720s references is rendered in figures 5.12, 5.13, and 5.14. These overlaid profiles revealed an interesting possibility in the time evolution of the crater. It was observed that the second hump, which showed up at 720s machining time, could be naturally included in the crater evolution of the tools and not be considered as a random occurrence (as it was first thought). This particular finding can be observed at 600-800 microns from the trailing edge in three overlaid figures.

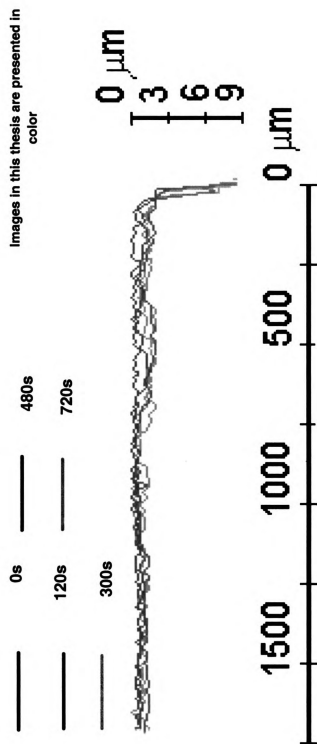


Figure 5.12 Time evolution of crater wear at the 300 s reference (5X objective)

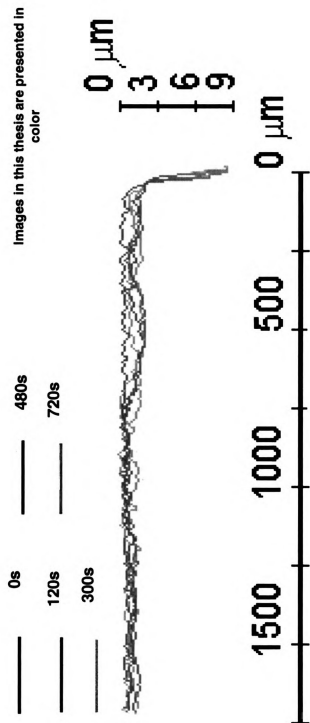


Figure 5.13 Time evolution of crater wear at the 300 s reference (5X objective)

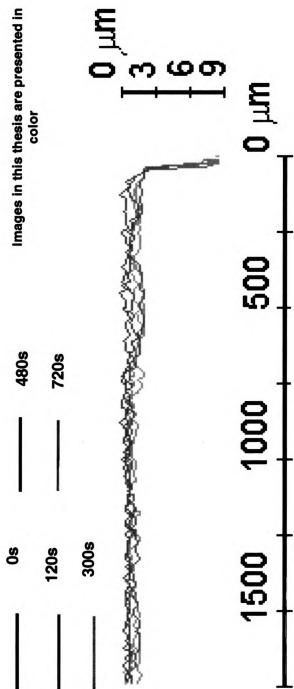


Figure 5.14 Time evolution of crater wear at the 720 s reference (5X objective)

5.3 ATOMIC FORCE MICROSCOPE RESULTS

The data obtained with the AFM, which was done for the 300s corner only, showed a good correspondence with the maximum depth value obtained with the 50x objective (2.6 microns). This was inferred from the fact that all AFM depth values observed were always within the z range of 2.5 μm , with the exception of the images gathered next to the inland side limit of the crater. In the latter, some zones were considered out of the z-range by the Nanoscope II software meaning that in these particular areas the depth was bigger than 2.5 μm . The AFM 3D images showed the presence of two mountain-shape formations in both limits of the crater zones. Also, the presence of the depression next to formation in the edge side of crater zone was detected. Based on the x-ray analysis, the AFM findings, and the position of these formations it is speculated that they are steel particles attached to the TiN coating. Appendix F contains the more relevant information regarding AFM data.

5.4 FLANK WEAR EVOLUTION AND MEASUREMENTS

The flank BSE images of the new corner and the corner with 480s machining time helped to define approximately some important reference points in the flank (Appendix G). These BSE images showed that Al_2O_3 was already exposed on the tip of the new insert. The Al_2O_3 distance, measure on the flank face with the SIS 3.0 software, was 34 microns and was probably the result of the finishing process (honing) for the insert edge. The Al_2O_3 flank distance increases to 36.53 microns at 480s machining time and exhibits scoring marks as well as some steel

particles attached. The TiN flank layer in the 480s corner appeared to be worn slightly in a distance of 25.85 microns and also exhibited scoring marks plus steel particles attached.

As mentioned in 4.2.4 2D and 3D confocal images were not gathered and phi-z sections (x-z) were obtained instead. In the aim of extracting a time evolution of the flank wear the flank profiles were rendered in a time sequence (Figures 5.15 through 5.17) and the slope values measured (Tables 5-3, 5-4, and 5-5). However, it is suspected that the scoring marks, the presence of steel particles attached, and the fact these measurements were done in different inserts an evolution trend was not clearly detected. In other words, although the flank wear evolution could be observed as machining time elapses, the slope measurements did not show a behavior that could be clearly related to the wear mechanisms and the coating wear-resistant properties. The slope values are plotted against machining time from figure 5.18 to 5.23.

Images in this thesis are presented in color

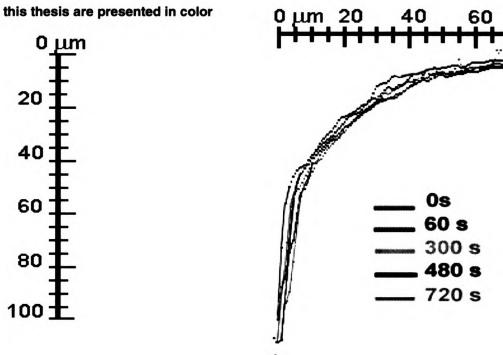


Figure 5.15 Flank wear evolution at the 300 s reference (50X objective)

Images in this thesis are presented in color

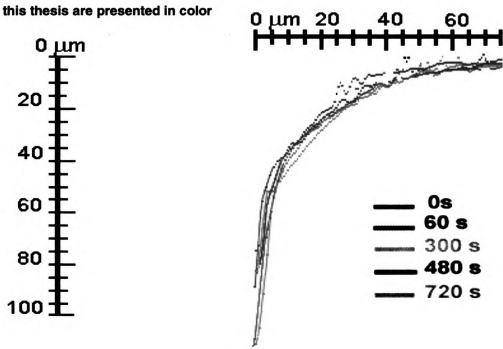


Figure 5.16 Flank wear evolution at the 480s reference (50 X objective)

Images in this thesis are presented in color

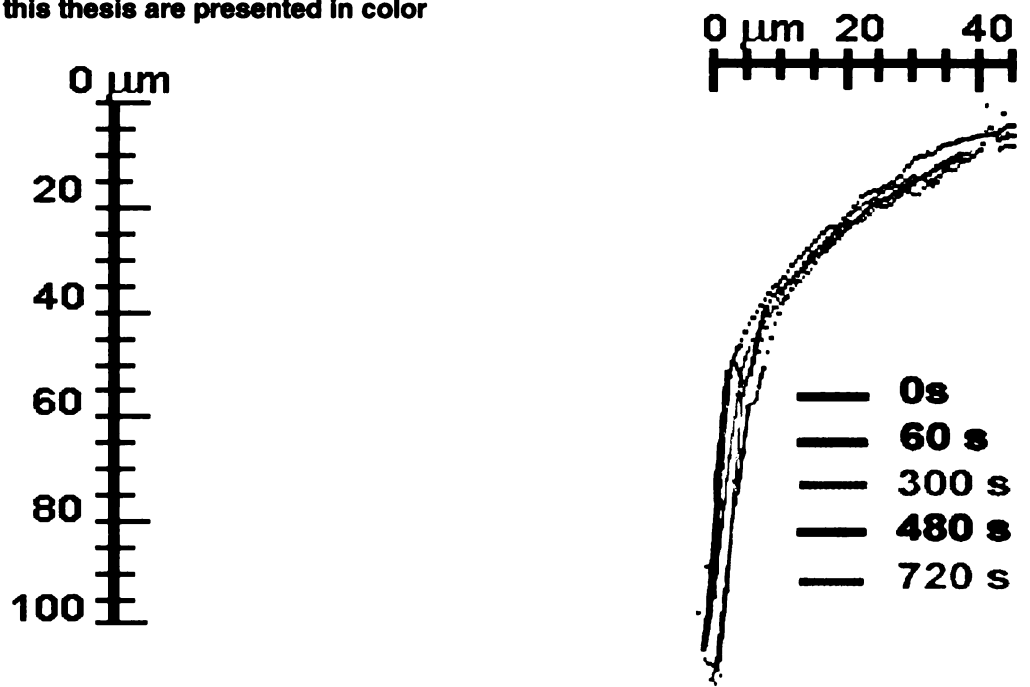
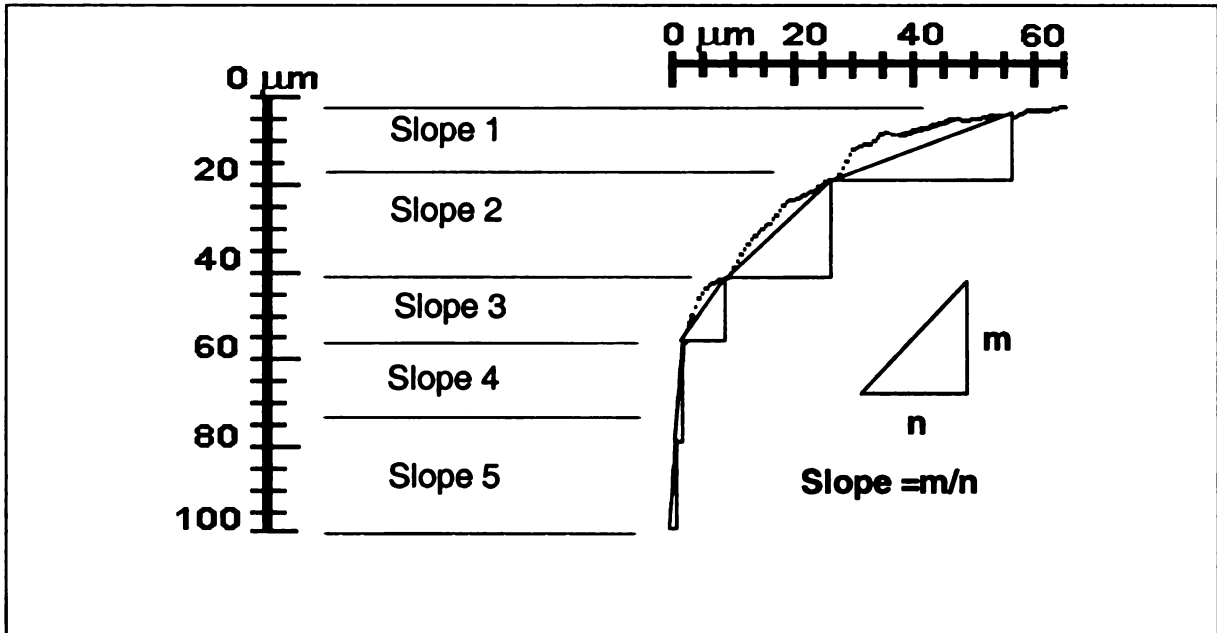


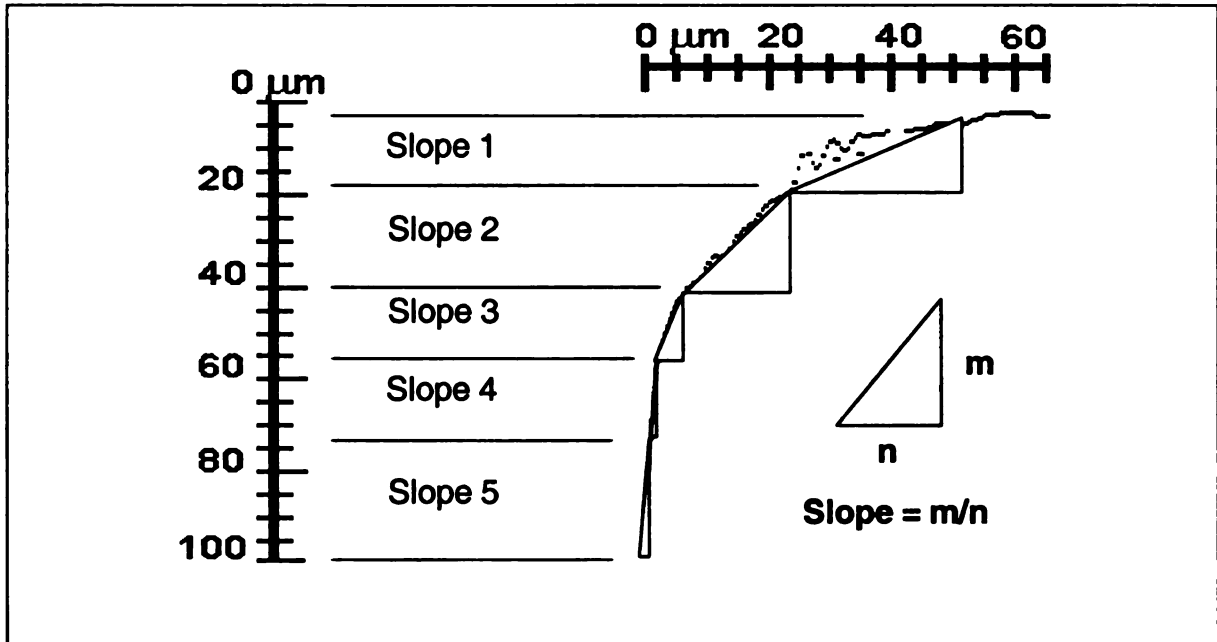
Figure 5.17 Flank wear evolution at the 720 s reference (50X objective)

Table 5-3 Time evolution of slope values at the flank face for reference 300s



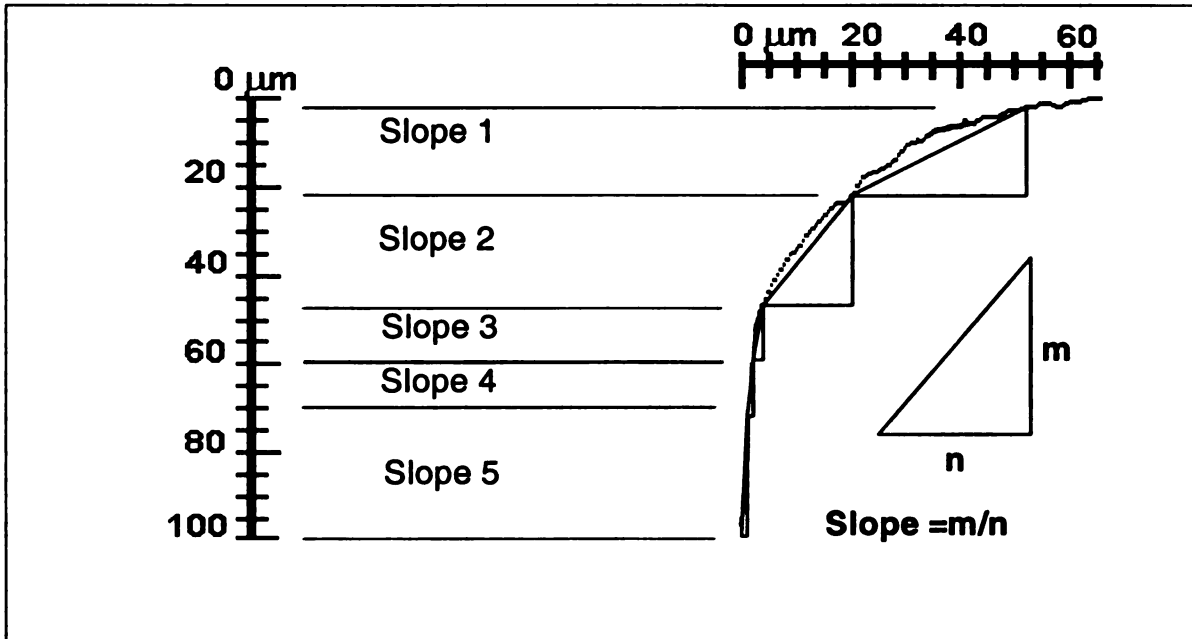
Machining Time	Slope 1	Slope 2	Slope 3	Slope 4	Slope 5
0	0.429	1.429	2.125	12.500	22.143
60	0.350	1.273	3.069	9.800	7.750
120	0.280	1.273	5.933	15.500	22.143
180	0.388	1.077	2.225	9.800	10.333
300	0.368	1.273	2.225	9.800	10.333
240	0.411	1.120	2.225	19.600	15.500
480	0.417	1.167	3.179	6.533	10.333
720	0.400	1.129	3.56	9.800	6.200

Table 5-4 Time evolution of slope values at the flank face for reference 480s



Machining Time	Slope 1	Slope 2	Slope 3	Slope 4	Slope 5
0	0.389	1.421	3.600	11.333	19.000
60	0.412	1.350	3.600	10.200	5.900
120	0.483	1.216	3.103	10.2	10.2
180	0.530	1.227	2.250	14.571	31.667
240	0.510	1.286	1.758	10.2	12.667
300	0.560	1.174	3.103	12.750	7.917
480	0.483	1.174	3.913	8.5	38.000
720	0.448	1.174	3.000	20.5	19.000

Table 5-5 Time evolution of slope values at the flank face for reference 720s



Machining Time	Slope 1	Slope 2	Slope 3	Slope 4	Slope 5
0	0.630	1.564	6.364	14.75	24.429
60	0.485	1.531	2.692	14.75	11.4
120	0.427	1.838	8.750	14.75	6.840
180	0.465	1.515	3.5	11.8	17.1
240	0.475	1.47	5.000	14.75	10.688
300	0.518	1.361	5.384	14.75	21.375
480	0.435	1.838	3.5	14.75	8.5
720	0.430	2.1	3.5	29.5	15.545

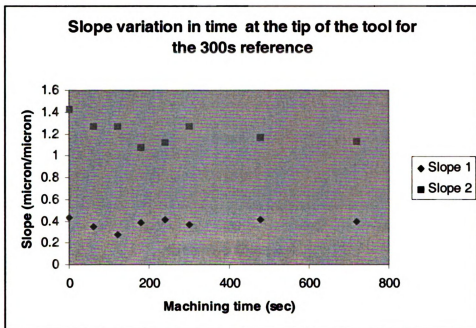


Figure 5.18 Plot of slopes 1 and 2 versus machining time (300 s ref.)

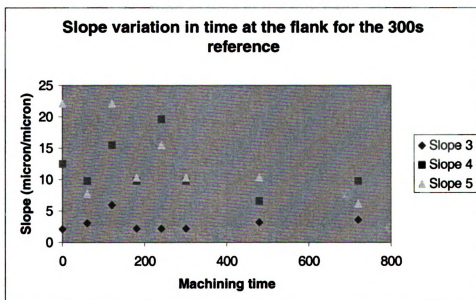


Figure 5.19 Plot of slopes 3, 4, and 5 versus machining time (300 s ref.)

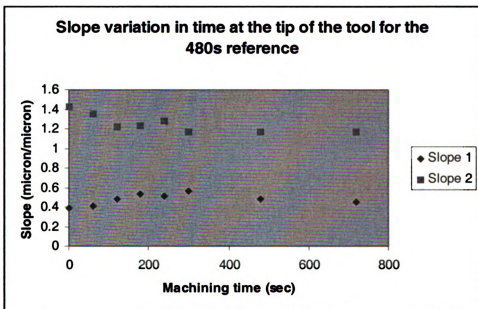


Figure 5.20 Plot of slopes 1 and 2 versus machining time (480 s ref.)

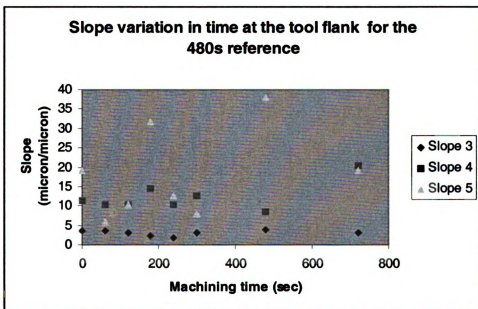


Figure 5.21 Plot of the slopes 3, 4, and 5 versus machining time (480 s ref.)

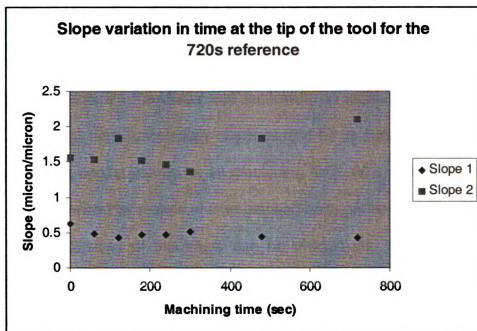


Figure 5.22 Plot of slopes 1 and 2 versus machining time (720 s ref.)

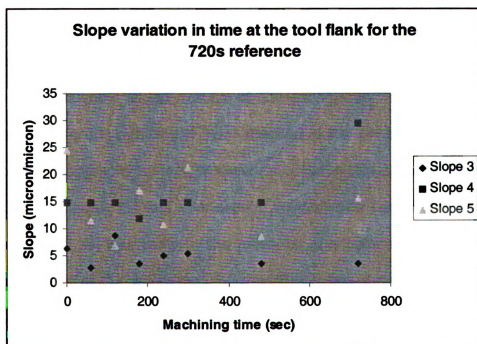


Figure 5.23 Plot of slopes 3, 4, and 5 versus machining time (720s ref.)

Chapter 6 : SUMMARY AND CONCLUSIONS

The present work studied the use of a Confocal Laser Scanning Microscope (CLSM) to characterize the crater and flank wear in multi-layer coated carbide tools. Crater wear was successfully characterized by its surface topography and maximum crater depths values for all machining time. Whereas, flank wear was partially characterized by means of time-elapsd flank profiles.

The major conclusions of this study can be divided into two categories: The microscopy aspect and the tool wear aspect. However, in most of the conclusions they are closely related. In the microscopy aspect the usefulness of confocal microscopy to obtain reliable surface profiles and topography was confirmed [29,30]. The need of validation methods [30] was also corroborated as SEM and AFM microscopes were used to determine the layers' limits and validate the depth values. Also, the optical properties of the materials were found to have an influence in the results of the topography rendering. This was especially true for the particles of steel attached to the TiN layer, which seemed to distort the topography surface wherever a considerable accumulation of steel was found. Regarding the tool wear aspect, the particular behavior of the wear in coated tools [33,34] was verify by the presence of a humped island of TiN and growing crater of Al_2O_3 with a maximum depth location changing with machining time. More representative crater wear profiles could be obtained if they are obtained parallel to the chip flow direction instead of the direction perpendicular to the trailing edge. The use of different corners to analyze the tool wear evolution seems to had a bigger impact in flank wear than in crater wear, and this

was reflected in the difficulties to find a flank wear trend. The need for automated methods to get quantitative information of the worn zones from the images provided by the CLSM and SEM was also noted. This was especially evident when trying to discriminate the limits between the first and second layers.

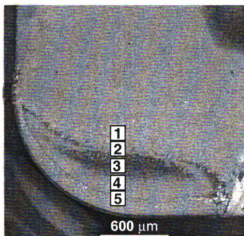
APPENDICES

APPENDIX A : SEM merged image of crater wear



Figure A.1 SEM merged images of crater wear for the corner with 300s machining time

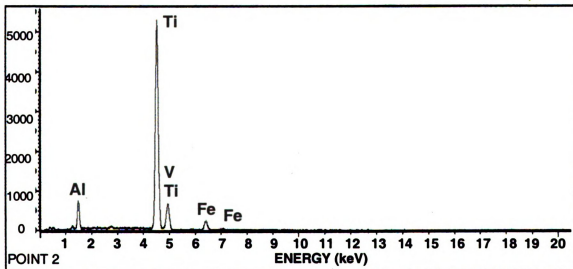
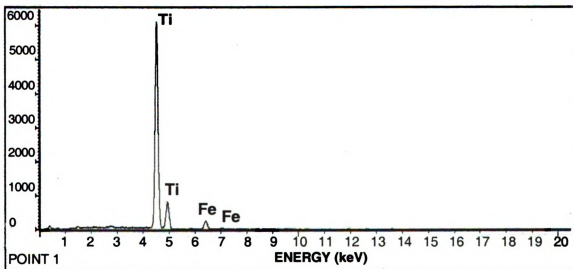
APPENDIX B: EDS spectral analysis and x-ray dot maps



Sample ID : M-BSE-300s
Area ID : Crater
Label : Spectra Analysis
Date/Time : 2004/05/14

Note :

Each area has its own spectral analysis identified by point 1, 2, 3, 4, and 5 in the graphs Counts versus Energy



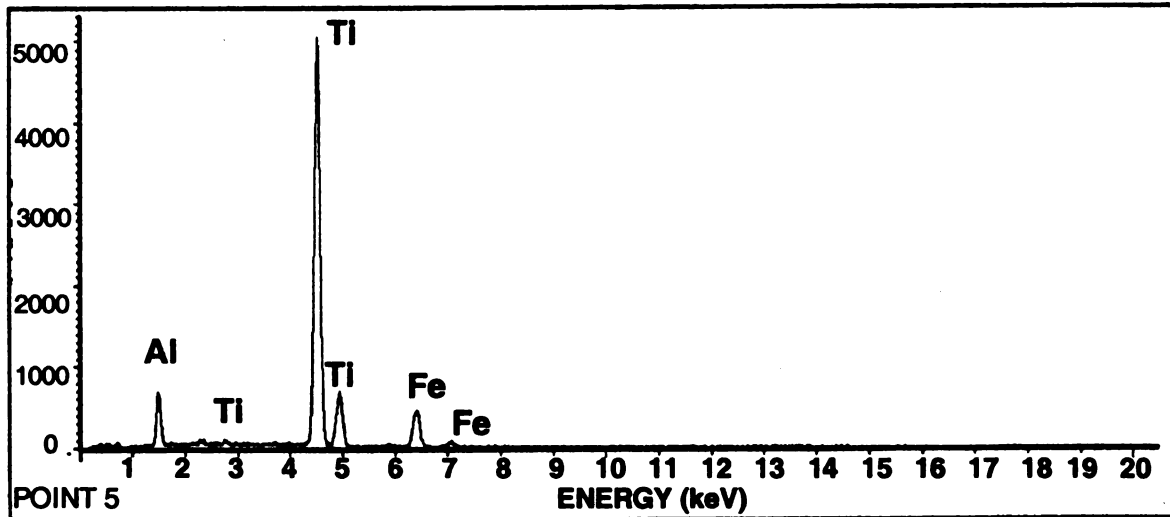
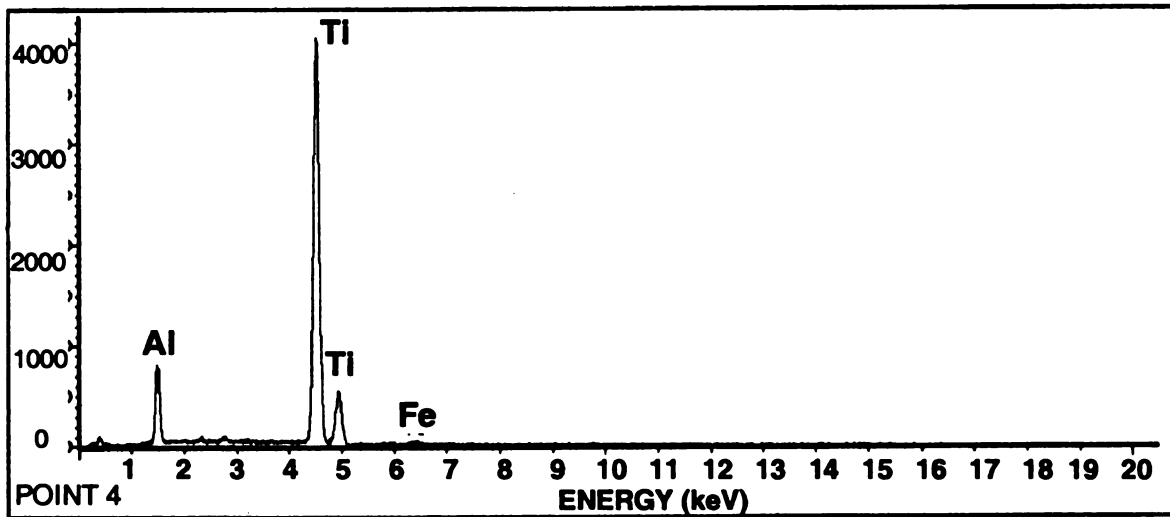
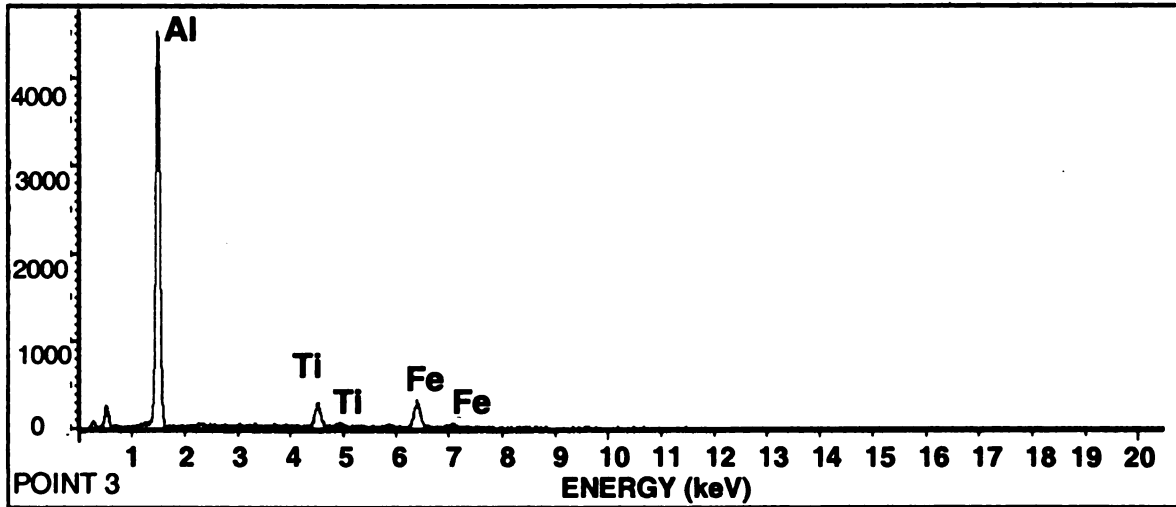
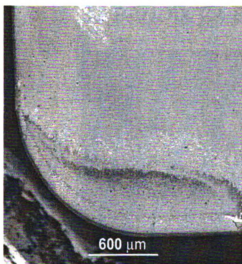


Figure B.1 EDS chemical spectral analysis for the corner with 300s machining time



Sample ID : M-BSE-300s
Area ID : Crater
Label : Dot map
Date/Time : 2004/05/14

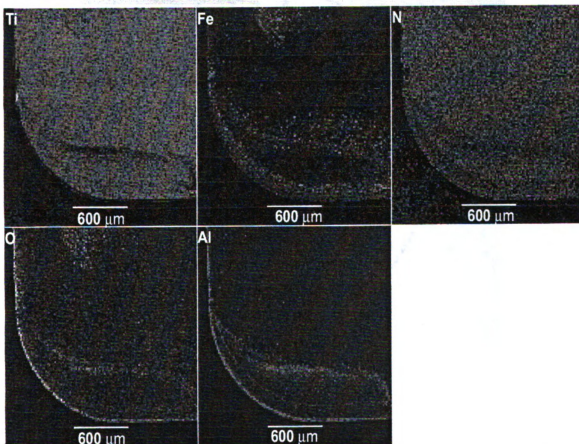


Figure B.2 X-ray dot maps of elements found for the corner with machining time of 300s

APPENDIX C : BSE images of crater wear

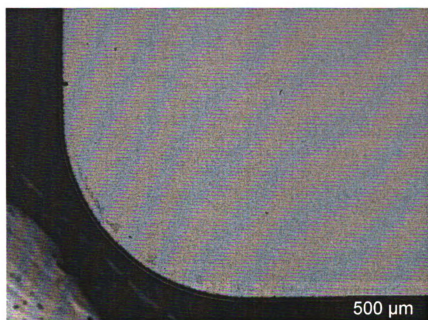


Figure C.1 BSE image of crater wear for 0 s machining time (New insert)

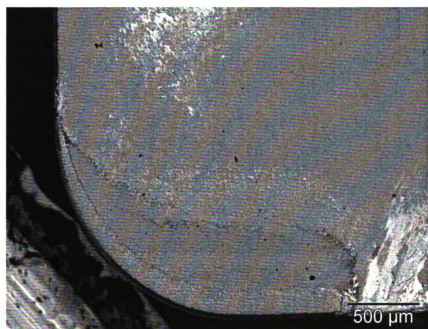


Figure C.2 BSE image of crater wear for 60 s machining time

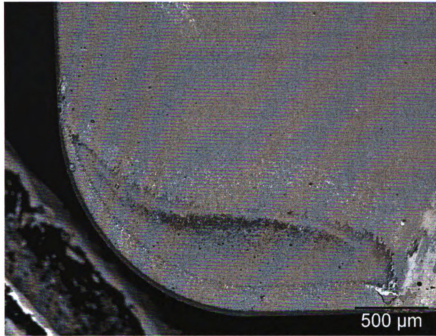


Figure C.3 BSE image of crater wear for 120 s machining time

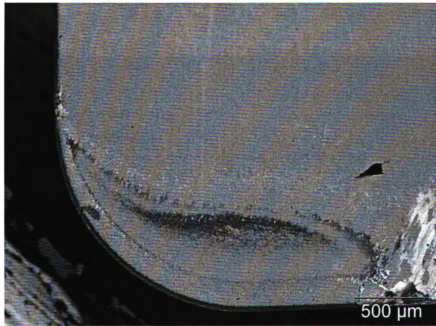


Figure C.4 BSE image of crater wear for 180 s machining time

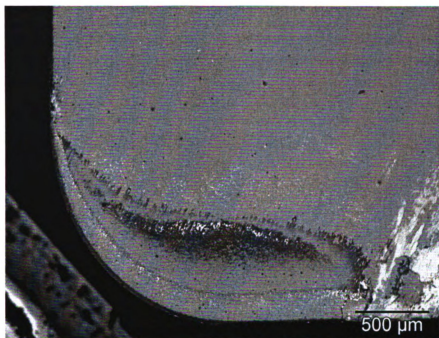


Figure C.5 BSE image of crater wear for 240 s machining time

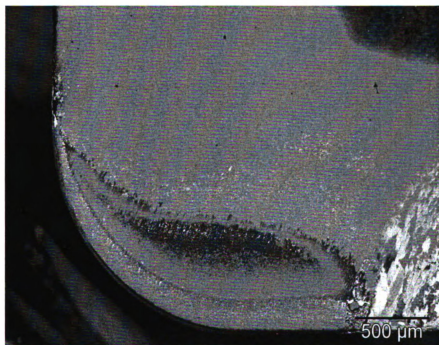


Figure C.6 BSE image of crater wear for 300 s machining time

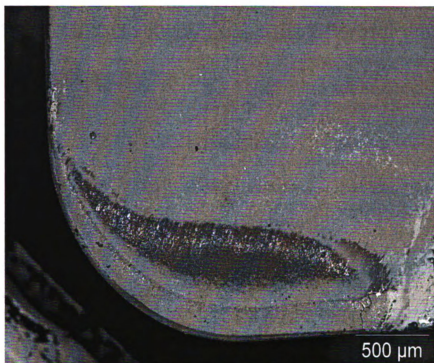


Figure C.7 BSE image of crater wear for 480 s machining time

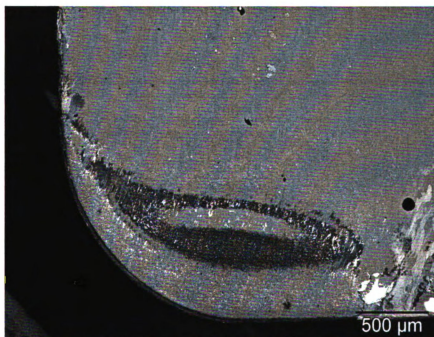
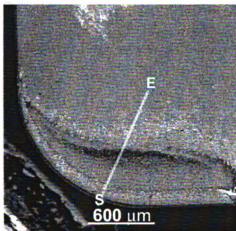


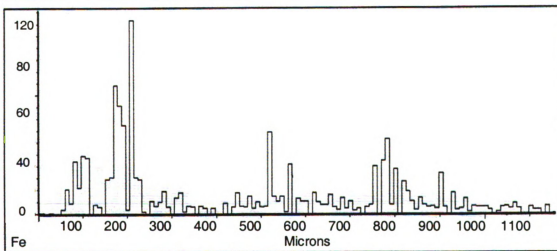
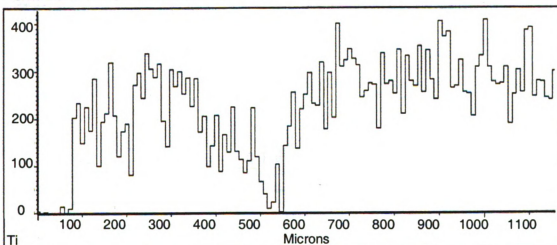
Figure C.8 BSE image of crater wear for 720 s machining time

APPENDIX D : X-ray linescans of crater wear



Sample ID : M-BSE-300s
Area ID : Crater
Label : Linescan
Date/Time : 2004/05/14

Each chemical element is identified with its symbol in the graphs Counts versus Distance (microns)



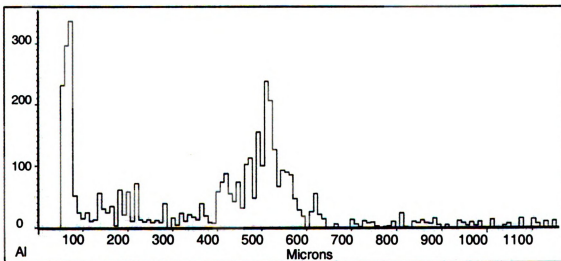
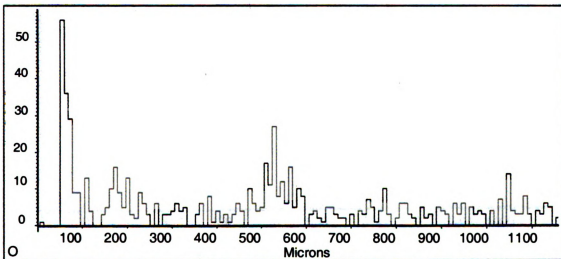
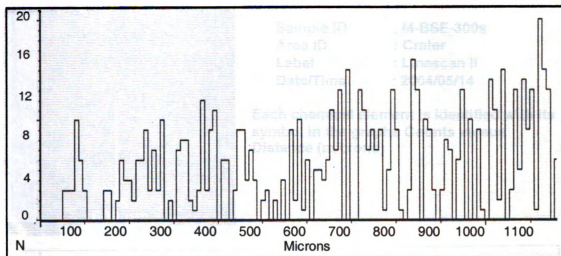
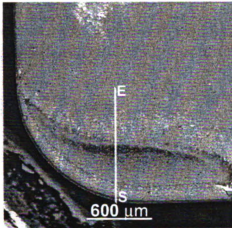
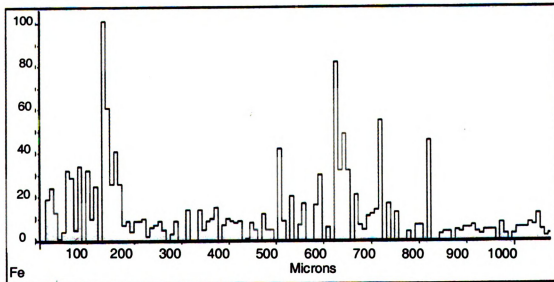
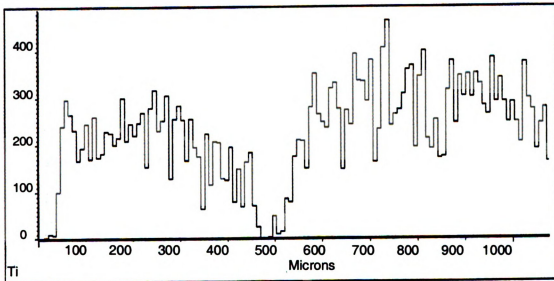


Figure D.1 Linescan chemical analysis of crater wear parallel to the chip flow (300s machining time)



Sample ID : M-BSE-300s
 Area ID : Crater
 Label : Linescan ii
 Date/Time : 2004/05/14

Each chemical element is identified with its symbol in the graphs Counts versus Distance (microns)



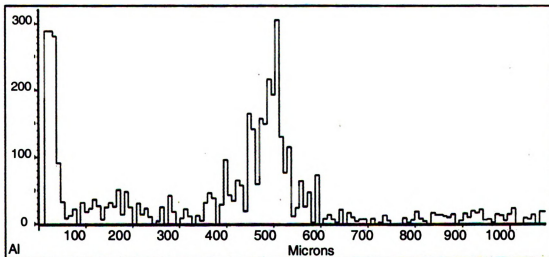
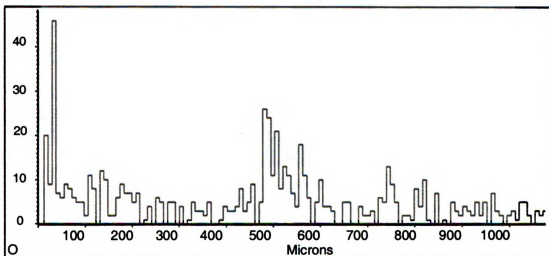
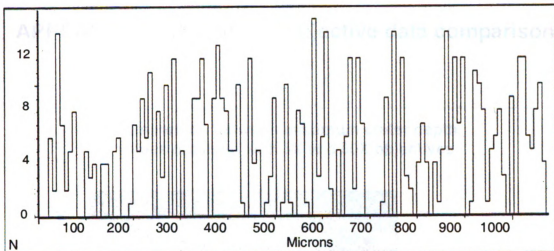


Figure D.2 Linescan chemical analysis of crater wear perpendicular to the trailing edge (300s machining time)

APPENDIX E : 5X and 50X objective data comparison

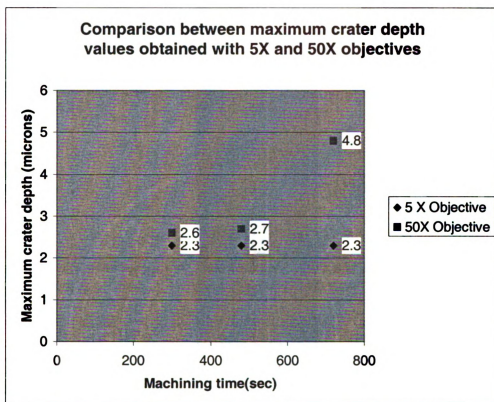


Figure E.1 Plot of the maximum crater wear depth comparison between the 5X and 50X objectives



Figure E.2 Phi-z section of crater wear for 300s machining time at the maximum depth location



Figure E.3 Phi-z section of crater wear for 480 s machining time at the maximum Depth location



Figure E.3 Phi-z section of crater wear for 720s machining time at the maximum depth location

APPENDIX F: Atomic Force Microscope Images



Figure F.1 AFM merged images in the maximum crater wear zone at 300s machining time

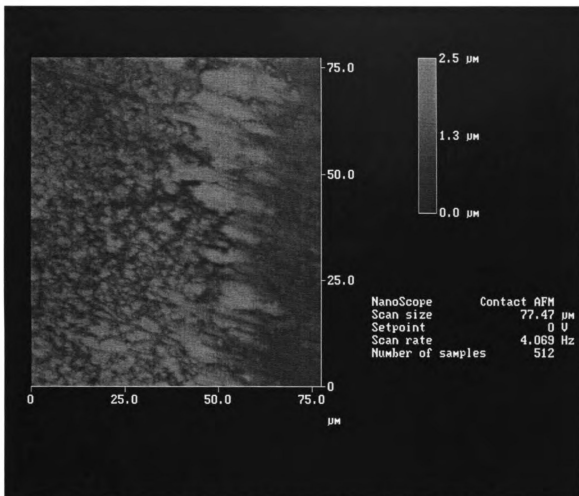


Figure F.2 AFM 2D view of zone B for 300s machining time

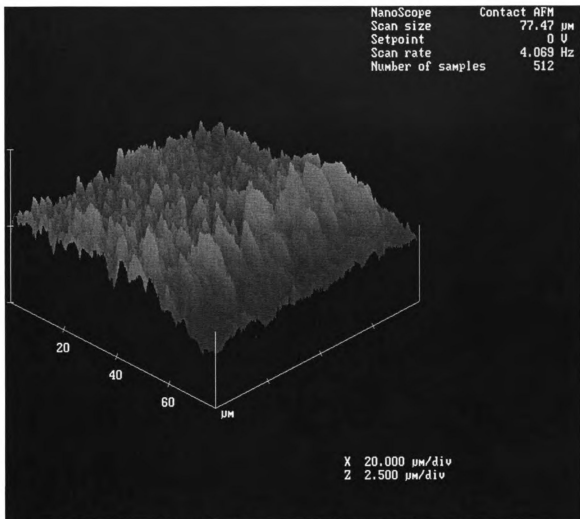


Figure F.3 AFM 3D view of the zone B for 300s machining time

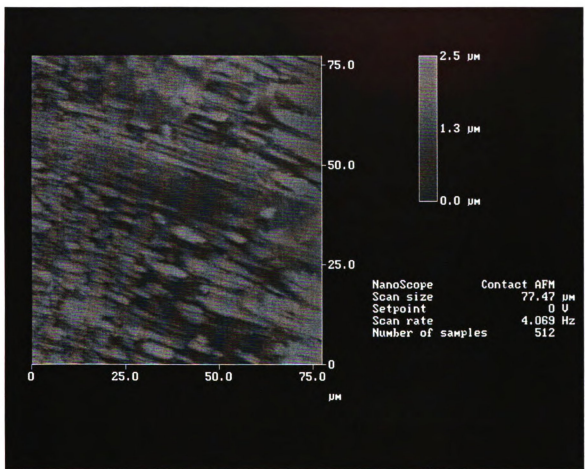


Figure F.4 AFM 2D view of the zone K for 300s machining time

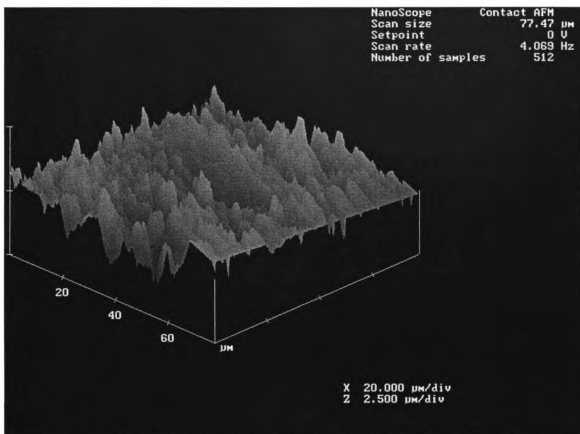


Figure F.5 AFM 3D view of the zone K for 300s machining time

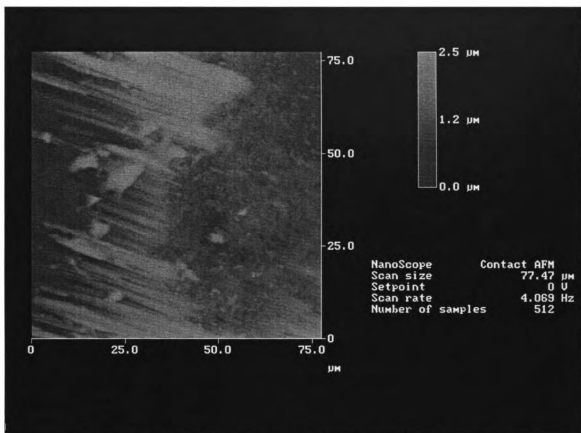


Figure F.6 AFM 2D view of the zone M for 300s machining time

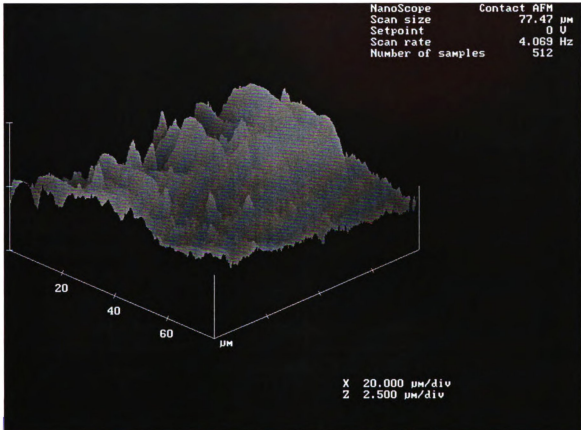


Figure F.7 AFM 3D view of the zone M for 300s machining time

APPENDIX G: BSE images of the flank face

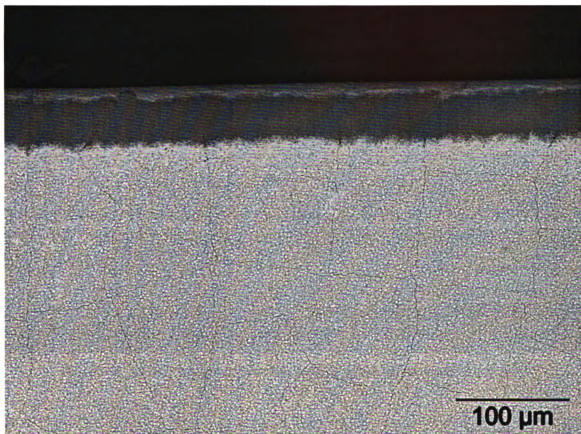


Figure G.1 BSE image of the flank face for an unworn insert

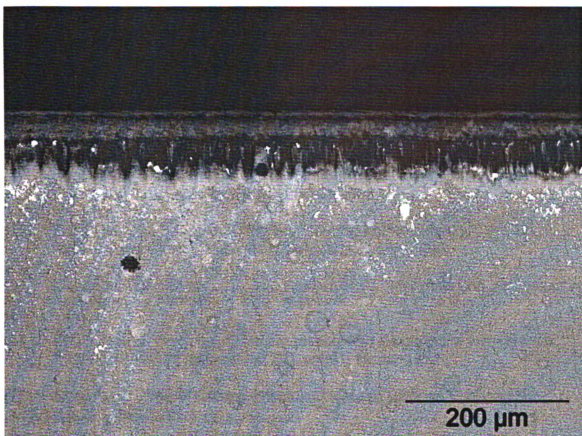


Figure G.1 BSE image of the flank face after 480s machining time

BIBLIOGRAPHY

- [1] Groover, M.P., "Fundamentals of Modern Manufacturing", Prentice Hall Inc., p.p. 543, 545-6, 1996
- [2] Schey, J.A., "Introduction to manufacturing processes", 3rd Ed., McGraw-Hill companies Inc., p.p. 663-664, 2000
- [3] Boothroyd, G. and Knight, W.A., "Fundamentals of machining and machining tools", 2nd Ed., p.p. 129-134, 1989
- [4] Kalpakjian, S., "Manufacturing Engineering and technology", 3rd Ed., Addison and Wesley Publishing Company, p.620, 1995
- [5] Degarmo, E.P., Black, J.T., and Kosher, R.A., "Materials and processes in manufacturing", 8th Ed., p. 639, 1997
- [6] ISO 5 th Draft Proposal, "Tool life testing with Single-point turning tools", ISO/TC 29/WG22 (Secretariat 37), vol.91, March 1972
- [7] Shaw, M.C., "Metal Cutting Principles", Oxford Science Publications, p.p.225, 239, 1991
- [8] Childs, T.H.C., Maekawa, K., Obikawa, T., and Yamane, Y., "Metal Machining", Arnold Publishers, p.p.76, 132,
- [9] Naerheim, Y. and Trent, E.M., "Diffusion wear of cemented carbide tools when cutting steel at high speeds", Metals Technology 4, p.p. 548-556, 1977
- [10] Kwon, P., "Theoretical Foundations for the optimization of ceramic coated tools", Master of Science dissertation, MIT, 1985, p.p. 14, 42-43
- [11] Kim, W.S., "A new methodology for predictive tool wear", PhD dissertation, Michigan State University, p.p. 15, 2000
- [12] Kramer, B.M. and Suh, N.P., "Tool wear by solution: A quantitative understanding", Journal of Vacuum Science and Technology, vol. A3 (6) Nov/Dec, p.p. 2439-2444, 1985
- [13] Ventakesh, V.C., "Performance Evaluation of TiC Coated Solid TiC Tools", Annals of the CIRP, 1983, 32, 101-4

- [14] Li, X.S. and Low, I., "Advanced Ceramic Tools for Machining Application I", Key Eng. Materials, Transtech Publications, Switzerland, p. 10, Vol. 96, 1994
- [15] Smith, A.B. and Whittle, N.C., "Effect of CVD Titanium Nitride Coating on the Cutting Properties of High Speed Steel Tools", Proceedings of the Twenty-Fifth International Machine Tool design and Research Conference, Birmingham, April 1985, edited by S.A. Tobias, Macmill Publishers Limited, London, 261-268
- [16] Vaidyanathan, P.N., "Ceramic coatings for cutting tools applications", Ceramic Engineering and Science proceedings, 1988, 9, [9-10], 1209-1214
- [17] Posti, E. "Influence of coating thickness on the life of TiN-Coated High Speed Steel Cutting Tools", Wear, 1989, 129, 273-283
- [18] Shanshal, D., "Effect of a nitride coating on the life of cutting tools", Dissertation Abstracts International, 1989, 49, [9], 3967-B
- [19] Takatsu, S., "Coated cemented Carbide Cutting tools", Sintering '87, Vol. 2, Tokyo, Japan, 4 – 6, November, 1987, 1263-1268
- [20] Flegler, S.L., Heckman, J.W. and Klomparens, K.L., "Scanning and transmission electron microscopy. An introduction", Oxford University Press, p.p. 5-6, New York, 1993
- [21] Corle, T.R. and Kino, G.S., "Confocal Scanning Microscopy and related imaging systems", Academic Press, San Diego, CA, 1996, p.p.7-9, 31-32
- [22] Microscope-microscope.org: Microbus (2003)," Microscope glossary", from [http:// www.microscope-microscope.org/basic/microscope-glossary.htm](http://www.microscope-microscope.org/basic/microscope-glossary.htm)
- [23] Whallon, J.H., "Introduction to laser scanning confocal microscopy", Center of Advanced Microscopy, Michigan State University, 2001, p.p.1.8-1.10, 4.4-4.5
- [24] Hetch, E. and Zajac, A., "Optics", Addison and Wesley, 1979
- [25] Ladic, L., "3D laser scanning confocal microscopy", Dept. of Physiology, U.B.C., Copyrigh 1995, from: <http://www.cs.ubc.ca/spider/ladic/overview.html>

- [26] Gee, M.G. and McCormick, N.J., "The application of confocal scanning microscopy to the examination of ceramic wear surfaces", *Journal of Applied Physics* 25, A230-A235, 1992
- [27] Devillez, A., Lesko, S. and Mozer, W., "Cutting tool crater wear measurement with white-light interferometry", *Wear* 256, p.p. 56–65, 2004
- [28] Anamalay, R.V., Kirk, T.B. and Panzera, D., "Numerical descriptors for the analysis of wear surfaces using laser scanning confocal microscopy", *Wear* 181-183, p.p. 771-776, 1995
- [29] Hanlon, D.N., Todd, I., Peekstok, E., Rainforth, W.M., Van der Zwaag, S., "The application of laser scanning confocal microscopy to tribological research", *Wear* 251, p.p. 1159-1168, 2001
- [30] Wessel, S., Pagel, S., Ritter, M., Hohenberg, H., and Wepf, R., "Topographic measurements of real structures in reflection confocal laser scanning microscope (CLSM)", *Microscope Microanalysis* Vol. 9, suppl. 3, 162, 2003.
- [31] Dawson, T.J. and Kurfess, T.I., "Wear trends of PCBN cutting tools in hard turning", from:
http://www.hardinge.com/hardium/PDF/Dawson_NAMRC_2002.pdf
- [32] C. Godoy, R. F. Ávila, F. C. Marinho, M.M. Lima, A. M. Abrão, E. M. Paula e Silva, "Análise Topográfica por Perfilometria do Desgaste de Cratera em Ferramenta de Metal Duro Revestida com TiN", *Matéria*, Vol 8, Nº 2 (2003) 145 – 154,
- [33] Chubb, J.P. and Billingham, J., "Coated cutting tools- A study of wear mechanisms in high speed machining", *Wear*, vol. 61, pp. 283-293
- [34] Kountanya, R.K., "Predictive Tool wear of coated tools systems", M.S. Thesis, Michigan State University, 1998
- [35] Kennametal Inc. - Online catalog (2004) from:
http://www.kennametal.com/en/new_catalog/catalog_frame.jhtml

MICHIGAN STATE UNIVERSITY LIBRARIES



3 1293 02504 3187